Halo masses for optically-selected and for radio-loud AGN from clustering and galaxy-galaxy lensing

Rachel Mandelbaum[1]⋆, Cheng Li[2,3]†, Guinevere Kauffmann[2]‡, Simon D. M. White[2]

[1] *Institute for Advanced Study, Einstein Drive, Princeton NJ 08540, USA*
[2] *Max-Planck-Institute for Astrophysics, Karl-Schwarzschild-Str. 1, D-85741 Garching, Germany*
[3] *MPA/SHAO Joint Center for Astrophysical Cosmology at Shanghai Astronomical Observatory, Nandan Road 80, Shanghai 200030, China*

ABSTRACT
We compute two-point correlation functions and measure the shear signal due to galaxy-galaxy lensing for 80 000 optically identified and 5 700 radio-loud AGN from Data Release 4 (DR4) of the Sloan Digital Sky Survey. Halo occupation models are used to estimate halo masses and satellite fractions for these two types of AGN. The large sample size allows us to separate AGN according to the stellar mass of their host galaxies. We study how the halo masses of optical and radio AGN differ from those of the parent population at fixed M_*. Halo masses deduced from clustering and from lensing agree satisfactorily. Radio AGN are found in more massive halos than optical AGN: in our samples their mean halo masses are 1.6×10^{13} and $8 \times 10^{11}h^{-1}M_\odot$, respectively. Optical AGN follow the same relation between stellar mass and halo mass as galaxies selected without regard to nuclear properties, but radio-loud AGN deviate significantly from this relation. The dark matter halos of radio-loud AGN are about twice as massive as those of control galaxies of the same stellar mass. This boost is independent of radio luminosity, and persists even when our analysis is restricted to field galaxies. The large-scale gaseous environment of the galaxy clearly plays a crucial role in producing observable radio emission. The dark matter halo masses that we derive for the AGN in our two samples are in good agreement with recent models in which feedback from radio AGN becomes dominant in halos where gas cools quasi-statically.

Key words: galaxies: active – galaxies: haloes – galaxies: formation – gravitational lensing – dark matter –large-scale structure of Universe

1 INTRODUCTION

It is now widely accepted that galaxies form by the cooling and condensation of baryons within a merging hierarchy of dark matter halos (White & Rees 1978). Processes other than cooling also influence the relationship between galaxies and their halos. "Feedback," both from supernova explosions and from energy liberated during the accretion of material onto a central supermassive black hole, is currently under considerable scrutiny and debate, because it is believed to play a very important role in regulating the fraction of available baryons that end up in galaxies.

Over the past few years, considerable effort has been devoted to obtaining quantitative constraints on the relationship between galaxies and their dark matter halos us-

ing a variety of different methods. Models that describe the evolved, non-linear dark matter distribution in terms of its halo building blocks (so-called halo models, e.g. Peacock & Smith 2000; Seljak 2000; Berlind & Weinberg 2002; Cooray & Sheth 2002; Yang et al. 2003) or direct N-body simulations (e.g. Kauffmann et al. 1997; Jing et al. 1998; Kauffmann et al. 1999; Benson et al. 2000; Yang et al. 2003), can be used in conjunction with the measured clustering amplitude of galaxies to constrain the relationship between the galaxies and their host halos. These constraints should be regarded as indirect, in part because of the need for a cosmology-dependent conversion from galaxy bias to halo mass.

Weak lensing around galaxies (or galaxy-galaxy lensing, hereafter g-g lensing) provides a *direct* probe of the dark matter that surrounds galaxies (for a review, see Bartelmann & Schneider 2001). Gravitational lensing induces tangential shear distortions of background galaxies around foreground galaxies, allowing direct measurement of

⋆ E-mail: rmandelb@ias.edu, Hubble Fellow
† E-mail: leech@mpa-garching.mpg.de
‡ E-Mail: gamk@mpa-garching.mpg.de

the galaxy-mass correlation function around galaxies. The individual distortions are small (of order 0.1 per cent), but by averaging over all foreground galaxies within a given subsample, we obtain high signal to noise in the shear as a function of angular separation from the galaxy. If we know the lens redshifts, the shear signal can be related to the projected mass density as a function of proper distance from the galaxy. Thus we can observe the averaged DM distribution around any given galaxy sample.

These techniques have been applied to study how galaxies with different properties such as luminosity, stellar mass, colour, spectral type and morphology populate dark matter halos of different masses (Hoekstra et al. 2005; Heymans et al. 2006; Mandelbaum et al. 2006). The derived relations serve as important constraints on models of galaxy formation, but they do not directly constrain the physical processes that are responsible for creating the relations in the first place.

For example, Yang et al. (2005) use the occupation statistics of a group catalogue to show that the mean luminosity of halo central galaxies scales with halo mass as $L_c \propto M^{2/3}$ for halos less massive than $10^{13} h^{-1} M_\odot$, and flattens to a much shallower relation ($L_c \propto M^{1/4}$) for more massive halos. It has been proposed that this characteristic scale reflects the imprint of feedback from radio-loud AGN, which heat the gas in massive halos and prevent it from cooling and condensing onto the central galaxy. In the models of Croton et al. (2006) and Bower et al. (2006), this "radio mode" feedback operates in halos with masses greater than $\sim 3 \times 10^{11} h^{-1} M_\odot$, where cooling times are long compared to the free-fall time and gas cools quasi-hydrostatically. On the other hand, the work of Springel et al. (2005a) and Hopkins et al. (2005b,a) has focused on the role of optically luminous AGN in expelling gas from galaxies and regulating the rate at which they are able to form stars. In these models, the major growth phases of black holes and the triggering of optically luminous AGN occur when two galaxies that contain sufficient cold gas merge with each other. The triggering thus does not depend *directly* on the mass of surrounding dark matter halo.

In order to constrain the importance of these processes, it is important to understand how the AGN themselves are related to the surrounding dark matter distribution. The large-scale clustering amplitude of luminous quasars has been accurately measured using tens of thousands of such objects drawn from the 2dF and Sloan Digital Sky Survey. Croom et al. (2005) use a sample based on the 2dF to conclude that quasars from $0.5 < z < 2.5$ inhabit dark matter halos with a characteristic mass of $\sim 3 \times 10^{12} h^{-1} M_\odot$, and that this mass does not depend on redshift or on quasar luminosity. Myers et al. (2007a) use a photometrically-identified quasar sample from SDSS over a similar redshift range to estimate a typical mass of $\sim 5 \times 10^{12} h^{-1} M_\odot$, without a robust detection of luminosity-dependent bias at fixed redshift (for which there is only a marginal detection in the 2dF sample, Porciani & Norberg 2006). Several studies (Hennawi et al. 2006; Myers et al. 2007b, 2008) have also probed the very small-scale clustering of quasars, using pairs of binary quasars, which are a probe of how the local environment affects quasar activity, though no clear consensus arises from these studies. The Croom et al. (2005) results about halo masses were recently

extended to redshifts $z > 3$ by Shen et al. (2007) and $z < 0.6$ by Padmanabhan et al. (2008). The lack of evolution of the halo masses from the $\sim 10^{12} h^{-1} M_\odot$ scale is all the more remarkable considering that the nonlinear mass evolves by well over a factor of ten over the full redshift range probed by these studies.

Clustering measurements of radio-loud AGN have been considerably less accurate because many fewer redshifts have been available. Studies of the angular clustering of radio sources drawn from the wide-area surveys such as the NRAO VLA Sky Survey (NVSS) or the Faint Images of the Radio Sky at Twenty-centimetres (FIRST) survey show that radio-loud AGN are considerably more strongly clustered than quasars. The estimated halo masses are typically around $10^{13} - 10^{14} M_\odot$ (Overzier et al. 2003). Magliocchetti et al. (2004) computed the redshift-space correlation function for 820 nearby radio sources with redshifts from the 2dF, and derived a characteristic halo mass of $10^{13.4} M_\odot$. No difference was found in the clustering properties of AGN with different radio luminosities.

This paper focuses on a sample of 80 000 optically identified AGN and 5 700 radio-loud AGN drawn from the Data Release 4 (DR4) of the Sloan Digital Sky Survey. We compute two-point correlation functions and measure the shear signal due to g-g lensing for these two samples. The large sample size allows us to split the AGN into different bins in stellar mass and study how the dark matter halo masses of optical and radio AGN differ at a fixed value of M_*. Nearby radio-loud AGN have been shown to have significantly higher stellar masses than optically-identified AGN at the same redshift (Best et al. 2005b), so it is important to understand whether the derived halo masses simply track this difference or whether the dark matter halo affects either the ability of an accreting black hole to produce a jet or the detectability of the jet at radio wavelengths.

We also create control samples of non-AGN that are matched in stellar mass, redshift and morphology, and we use these control samples to investigate whether the halo masses of active galaxies differ from those of their counterparts chosen irrespective of their level of nuclear activity. Finally, the fact that the clustering and weak lensing analyses are carried out on the same set of galaxies allows us to evaluate the consistency of our constraints on dark matter halo mass obtained using the two methods.

We begin by outlining the theory behind the lensing and clustering measurements in section 2. We then describe the data used for the analysis, and the analysis procedure, in section 3. The results for optical and radio-loud AGN are presented in section 4, including lensing and clustering separately, followed by a joint analysis. We then summarize the key results and discuss their implications in sections 5 and 6, respectively.

2 THEORY

2.1 Galaxy-galaxy lensing

Galaxy-galaxy weak lensing provides a simple way to probe the connection between galaxies and matter via their cross-correlation function

$$\xi_{gm}(\vec{r}) = \langle \delta_g(\vec{x}) \delta_m(\vec{x} + \vec{r}) \rangle \qquad (1)$$

where δ_g and δ_m are overdensities of galaxies and matter, respectively, and in practice the mean is taken over some survey volume (in theory it is the average over a whole distribution, but we can only estimate its value using the fixed volumes that are available in reality). We will interchangably express correlation functions as functions of vectors $(\vec{r})$ and scalars (r) because of the assumption of statistical isotropy.

This cross-correlation can be related to the projected surface density

$$\Sigma(R) = \overline{\rho} \int \left[1 + \xi_{gm} \left(\sqrt{R^2 + \chi^2} \right) \right] d\chi \qquad (2)$$

(for $r^2 = R^2 + \chi^2$), where we ignore the radial window, which is much broader than the typical extent of the lens. This surface density is then related to the observable quantity for lensing,

$$\Delta\Sigma(R) = \gamma_t(R)\Sigma_c = \overline{\Sigma}(< R) - \Sigma(R), \qquad (3)$$

where the second relation is true only for a matter distribution that is axisymmetric along the line of sight. This observable quantity can be expressed as the product of two factors, a tangential shear γ_t and a geometric factor, the critical surface density

$$\Sigma_c = \frac{c^2}{4\pi G} \frac{D_S}{D_L D_{LS} (1 + z_L)^2} \qquad (4)$$

where D_L and D_S are angular diameter distances to the lens and source, D_{LS} is the angular diameter distance between the lens and source, and the factor of $(1 + z_L)^{-2}$ arises due to our use of comoving coordinates. For a given lens redshift, Σ_c^{-1} rises from zero at $z_s = z_L$ to an asymptotic value at $z_s \gg z_L$; that asymptotic value is an increasing function of lens redshift.

In practice, we measure the g-g weak lensing signal around a stacked sample of lenses to obtain the average $\Delta\Sigma(R)$ for the whole sample. This stacked lensing signal can be split into two terms that dominate on different scales. The 1-halo or Poisson term, which is determined by the dark matter halo in which the galaxy lives, dominates on scales typically below $\sim 1 h^{-1}$Mpc. The halo-halo term, which is determined by correlations between the galaxy and other dark matter halos, dominates on larger scales. The 1-halo term can be further split into two contributions. For central galaxies, which reside at the peak density of a dark matter halo that is not contained within another halo (a host halo), the Poisson term is simply determined by the matter density of that host halo, $\rho(r)$. For satellite galaxies, which reside in dark matter subhalos, there is a contribution from the density of the dark matter subhalo, but there is also a term on hundreds of kiloparsec scales due to the cross-correlation between the galaxy position and the *host* dark matter halo. Consequently, the lensing signal on $<\sim 0.3 h^{-1}$Mpc scales tells us about the dark matter halo in which the galaxy resides; the signal from $\sim 0.3 - 1 h^{-1}$Mpc reveals the local environment of the galaxy; and the signal on larger scales indicates the large-scale correlations of the galaxy sample.

We interpret the lensing signal statistically using a halo model, which allows us to determine both the typical halo mass M_{cent} for central galaxies in our galaxy sample, and also the satellite fraction α (the fraction of the sample located in subhalos within some more massive host dark matter halo). In this simple formulation of the halo model, we

assume that all central galaxies in our sample have a single halo mass M_{cent}, and that all satellite galaxies are distributed in halos with $M > 3M_{cent}$ with the number in a halo of given mass above this threshold $\propto M$. Tests of this halo model formulation using the lensing signal from N-body simulations (Mandelbaum et al. 2005b) clearly indicate that the best-fitting M_{cent} and α recover the true values to within ~ 10 per cent, provided that the distribution of central halo masses is relatively narrow (FWHM typically a factor of 6 or less). For a broader distribution of central halo masses, the best-fitting M_{cent} lies between the median and the mean of the distribution, but may differ from either one by as much as a factor of two. For more details of this halo model and its assumptions, see Mandelbaum et al. (2005b). In this work, we use this halo model without applying any correction for the (unknown) scatter between galaxy stellar mass and dark matter halo mass, but we will discuss the extent to which our assumptions about the width of the central halo mass distribution are likely to be correct.

2.2 Galaxy clustering

The clustering of galaxies is usually quantified using the two-point correlation function (2PCF, e.g. Peebles 1980), defined by

$$dP_{12} = \bar{n}^2 [1 + \xi(\vec{r})] dV_1 dV_2. \qquad (5)$$

Here $\bar{n}$ is the mean number density of galaxies, and dV_1 and dV_2 are the volumes of two infinitesimally small spheres centered at $\vec{x}_1$ and $\vec{x}_2$ with distance of $\vec{r} = \vec{x}_2 - \vec{x}_1$. By definition, dP_{12} is the joint probability that a galaxy lies in each of the spheres, and so the 2PCF $\xi(r)$ represents the excess probability of finding two galaxies separated by a distance $\vec{r}$, compared with the result obtained for a uniform random distribution. If $\xi(r) > 0$, then galaxies are said to be clustered. In galaxy redshift surveys, the 2PCF is measured in redshift space and usually expressed as functions of separations perpendicular (r_p) and parallel (π) to the line of sight. In many cases, the projected two-point correlation function, $w_p(r_p)$, is the more useful quantity, because it does not suffer from redshift-space distortions, and is thus directly related to the real-space correlation function. The 2PCF is also simple to compute and can be easily compared with the predictions of theoretical models.

The amplitude of the correlation function on scales larger than a few Mpc provides a direct measure of the mass of the dark matter halos that host the galaxies through the halo mass - bias relation. As shown in Li et al. (2008a,b), the amplitude of the correlation function on scales $\lesssim 100$ kpc can serve as a probe of physical processes such as mergers and interactions. On intermediate scales, the shape of the correlation function is sensitive to how galaxies are distributed *within* their dark matter halos.

The clustering signal must also be interpreted using some form of halo model. Following the approach adopted in our previous work, we interpret clustering results using the models of Li et al. (2006a) and Wang et al. (2006) which are based on direct N-body simulations. We have constructed a set of 100 mock galaxy catalogues from the Millennium Simulation (Springel et al. 2005b) with exactly the same observational selection effects as the SDSS DR4. The Millennium

Simulation uses 10^{10} particles to follow the dark matter distribution in a cubic region $500h^{-1}$ Mpc on a side. The cosmological parameters assumed are $\Omega_m = 0.25$, $\Omega_\Lambda = 0.75$, $\sigma_8 = 0.9$ and $h = 0.73$. We adopted the positions and velocities of the galaxies given in the catalogue of Croton et al. (2006), who implemented a semi-analytic model in order to track the formation and evolution of galaxies in the simulation. Physical properties of the galaxies, such as stellar masses and AGN status, are not taken from the semi-analytic model, however, but instead are assigned to each model galaxy using parametrized functions. The main such function relates the stellar mass of the galaxy to the mass of the halo at the epoch when the galaxy was last the central dominant object in its own halo, including scatter in that relation. Tests have shown that this procedure allows us to match accurately both the stellar mass function of SDSS galaxies and the shape and amplitude of their two-point correlations as a function of stellar mass (Li et al. 2006a; Wang et al. 2006).

In Li et al. (2006b, hereafter L06), we adapted this halo model to interpret the clustering of optically-identified AGN. In that paper, we computed the correlation functions of AGN and of control samples of *inactive* galaxies that had the same redshift and stellar mass distribution as the active galaxies. We found that on scales between 100 kpc and 1 Mpc, AGN are clustered more weakly than the inactive sample. We then introduced a simple model in which the probability of a galaxy of given stellar mass to be an AGN is enhanced if it is the central galaxy of its own halo, and showed that this model could provide a good fit to the data. In the best-fitting model, 84 per cent of all optical AGN are located at the centres of their own dark matter halos (i.e., $f_{cen} = 0.84$), whereas this is true for only 73 per cent of inactive galaxies.

We emphasize that while in principle, it would be easy to assume that α derived from the lensing analysis is simply $1 - f_{cen}$ from the clustering analysis, the relationship is not as straightforward as this. The clustering analysis starts from the assumption that the AGN and control samples derive from a parent population which matches the statistical properties of galaxies as a function of stellar mass (i.e., the stellar mass function and the clustering as a function of mass). Any halo model parameters such as f_{cen} are then introduced as a way of matching the observed AGN clustering by modifying the probability that each galaxy in the parent population is an AGN. In contrast, the lensing analysis does not assume that the AGN and control samples stem from identical parent populations. In future analyses with larger datasets, we will jointly model clustering and lensing with the same assumptions at the outset; here, we simply use pre-existing analysis pipelines that output quantities that should be reasonably (but not exactly) comparable. Even in the absence of a completely unified approach to modeling, there are many valuable conclusions that can be drawn from the lensing and clustering signals (e.g., if both the clustering and lensing signals for a particular sample are comparable to the signals for the controls, or if they are both quite different from the signals for the controls).

3 DATA AND SIGNAL MEASURES

3.1 Overview of SDSS

The data used here are obtained from the SDSS (York et al. 2000), an ongoing survey to image roughly π steradians of the sky, and follow up approximately one million of the detected objects spectroscopically (Eisenstein et al. 2001; Richards et al. 2002; Strauss et al. 2002). The imaging is carried out by drift-scanning the sky in photometric conditions (Hogg et al. 2001; Ivezić et al. 2004), in five bands ($ugriz$) (Fukugita et al. 1996; Smith et al. 2002) using a specially-designed wide-field camera (Gunn et al. 1998). These imaging data are used to create the source catalogue that we use in this paper. In addition, objects are targeted for spectroscopy using these data (Blanton et al. 2003c) and are observed with a 640-fiber spectrograph on the same telescope (Gunn et al. 2006). All of these data are processed by completely automated pipelines that detect and measure photometric properties of objects, and astrometrically calibrate the data (Lupton et al. 2001; Pier et al. 2003; Tucker et al. 2006). The SDSS has had seven major data releases (Stoughton et al. 2002; Abazajian et al. 2003, 2004, 2005; Finkbeiner et al. 2004; Adelman-McCarthy et al. 2006, 2007, 2008). In this paper we use data from the fourth of these releases(DR4; Adelman-McCarthy et al. 2006).

3.2 The AGN and control samples

3.2.1 *Optically-identified AGN*

The sample of optically-identified AGN is the same as that analyzed in L06 and Li et al. (2008b), in which the clustering of AGN on a variety of different scales was studied.

The base sample is composed of $\sim 4 \times 10^5$ objects for which data are publicly available through DR4 and which have been spectroscopically confirmed as galaxies with r-band magnitudes in the range $14.5 < r < 17.6$, redshifts in the range $0.01 < z < 0.3$, and absolute magnitudes in the range $-23 < M_{0.1_r} < -17$. Here r is the r-band Petrosian apparent magnitude corrected for foreground extinction, and $M_{0.1_r}$ is the r-band absolute magnitude corrected to its $z = 0.1$ value using the k-correct code of Blanton et al. (2003a) and the luminosity evolution model of Blanton et al. (2003b). A sample of $\sim 80,000$ AGN are selected from the subset of these galaxies with $S/N > 3$ in the four emission lines [O III]λ5007, Hβ, [N II]λ6583 and Hα, following the criteria proposed by Kauffmann et al. (2003). In the following analysis, we occasionally divide our sample into "weak" and "powerful" AGN using the quantity L[OIII]$/M_{bh}$, where L[OIII] is the extinction-corrected [OIII] line luminosity of the AGN and M_{bh} is the black hole mass estimated from the velocity dispersion of the galaxy using the relation given in Tremaine et al. (2002). As discussed in Heckman et al. (2004), this quantity can be viewed as a measure of the accretion rate onto the black hole relative to the Eddington rate.

We have also constructed two sets of 20 different control samples from the full parent sample of galaxies by matching a number of physical parameters regardless of nuclear activity. For the first set, four physical parameters are matched: redshift (z), stellar mass (M_*), concentration (R_{90}/R_{50}),

and stellar velocity dispersion (σ_*). For the second set, the 4000 Å break strength (D_{4000}) is also matched. The matching tolerances are $\Delta cz < 500$ km s^{-1}, $\Delta \log M_* < 0.1$, $\Delta \sigma_* < 20$ km s^{-1}, $\Delta R_{90}/R_{50} < 0.1$ and $\Delta D_{4000} < 0.05$.[1] In the first case, 28 per cent of the control galaxies are also included in the AGN sample; in the second case, the overlap fraction is higher, 37 per cent. In both cases, the match fraction is a slightly increasing function of stellar mass.

3.2.2 Radio-loud AGN

The National Radio Astronomy Observatory (NRAO) Very Large Array (VLA) Sky Survey (NVSS; Condon et al. 1998) and the Faint Images of the Radio Sky at Twenty centimeters (FIRST) survey (Becker et al. 1995) are two radio surveys that have been carried out in recent years using the VLA radio synthesis telescope at a frequency of 1.4 GHz. Best et al. (2005b) identified radio-emitting galaxies within the main spectroscopic sample of the SDSS data release 2 (DR2) by comparing these galaxies with a combination of these two surveys. The use of two radio surveys allowed a radio sample to be constructed that was both reasonably complete ($\sim$95 per cent) and highly reliable (it is estimated that $\sim$99 per cent of the sources in the catalogue are genuine radio galaxies rather than false matches). In this paper, we use an updated catalogue of 5 712 radio galaxies based on the SDSS data release 4 (DR4). The sample spans the same redshift range as the sample of optically-selected AGN, and the radio luminosities of the AGN range from 10^{23} to 10^{26} W Hz^{-1} (i.e., they are mainly FRI type systems).

We have used the parent galaxy catalogue to construct a set of five control samples that are closely matched in redshift, stellar mass and stellar velocity dispersion. The matching tolerances are the same as used to construct the optical AGN control samples. We do not additionally match in D_{4000}, because almost all galaxies at the relevant stellar masses are red, with a strong 4000 Å break. Of the control sample, 10.3 per cent of the galaxies are radio-loud AGN; for our higher stellar mass subsample ($\log(M_*/M_\odot) \geqslant 11.44$), the radio-loud AGN fraction is 16 per cent, whereas for the lower M_* subsample, it is 7 per cent.

3.3 Lensing analysis

3.3.1 Lensing source catalogue

The source sample used for the lensing analysis is the same as that originally described in Mandelbaum et al. (2005a). This source sample includes over 30 million galaxies from the SDSS imaging data with r-band model magnitude brighter than 21.8, with shape measurements obtained using the REGLENS pipeline, including PSF correction done via re-Gaussianization (Hirata & Seljak 2003) and with cuts designed to avoid various shear calibration biases. In addition to these, there are also uncertainties due to photometric redshifts and/or redshift distributions of background galaxies, as well as due to other issues affecting the calibration

of the lensing signal, such as the sky subtraction uncertainties, intrinsic alignments, magnification bias, star-galaxy separation, and seeing-dependent systematics. The overall calibration uncertainty was estimated to be eight per cent (Mandelbaum et al. 2005a), though the redshift calibration component of this systematic error budget has recently been decreased due to the availability of more spectroscopic data (Mandelbaum et al. 2008). With a total estimated lensing calibration uncertainty of $\sim$ 5 per cent, this systematic is subdominant compared to the statistical error and to the uncertainty derived from the model used to interpret the lensing signal.

3.3.2 Lensing signal computation

Here we briefly describe the computation of the lensing signal; for more detail, see Mandelbaum et al. (2005a). For each lens, we identify sources within 46 logarithmically-spaced annuli around the lens (in comoving transverse separation) from 20 h^{-1}kpc to 2 h^{-1}Mpc. The tangential ellipticity of the source relative to the lens is measured, in order to estimate the tangential shear. Lens-source pairs are assigned weights according to the error on the shape measurement via

$$w_{ls} = \frac{\Sigma_c^{-2}}{\sigma_s^2 + \sigma_{SN}^2} \tag{6}$$

where σ_{SN}^2 is the intrinsic shape noise and σ_s is the measurement error on the source galaxy ellipticity. The factor of Σ_c^{-2} optimally weights the signal by the noise in $\Delta\Sigma$ rather than in the shear.

Once we have computed these weights, we compute the lensing signal in each radial bin as a summation over lens-source pairs via:

$$\Delta\Sigma(R) = \frac{\sum_{ls} w_{ls} e_t^{(ls)} \Sigma_c}{2\mathcal{R} \sum_{ls} w_{ls}} \tag{7}$$

where the factor of 2 and the shear responsivity $\mathcal{R}$ relate our definition of ellipticity to the shear, using the formalism in Bernstein & Jarvis (2002). In practice, $\mathcal{R} \approx 1 - e_{rms}^2 \approx 0.86$.

There are several additional procedures that must be done when computing the signal (for more detail, see Mandelbaum et al. 2005a). First, the signal computed around random points must be subtracted from the signal around real lenses to eliminate contributions from systematic shear. In practice, this correction is negligible for the scales used in this work. Second, the signal must be boosted, i.e. multiplied by $B(R) = n(R)/n_{rand}(R)$, the ratio of the number density of sources relative to the number around random points, in order to account for dilution by sources that are physically associated with lenses, and therefore not lensed.

To determine errors on the lensing signal, we divide the survey area into 200 bootstrap subregions, and generate 2500 bootstrap-resampled datasets. These bootstrap-resampled datasets are also crucial for determining the statistical significance of differences between correlated subsamples of galaxies, because fitting the signal to the halo model on each resampled dataset allows us to determine how much any overlap between two galaxy samples leads to a correlation between the best-fitting halo model parameters for the two samples.

---

[1] This procedure is identical to that in L06, except that the control galaxies are selected from the full parent sample, rather than from the subset of inactive galaxies.

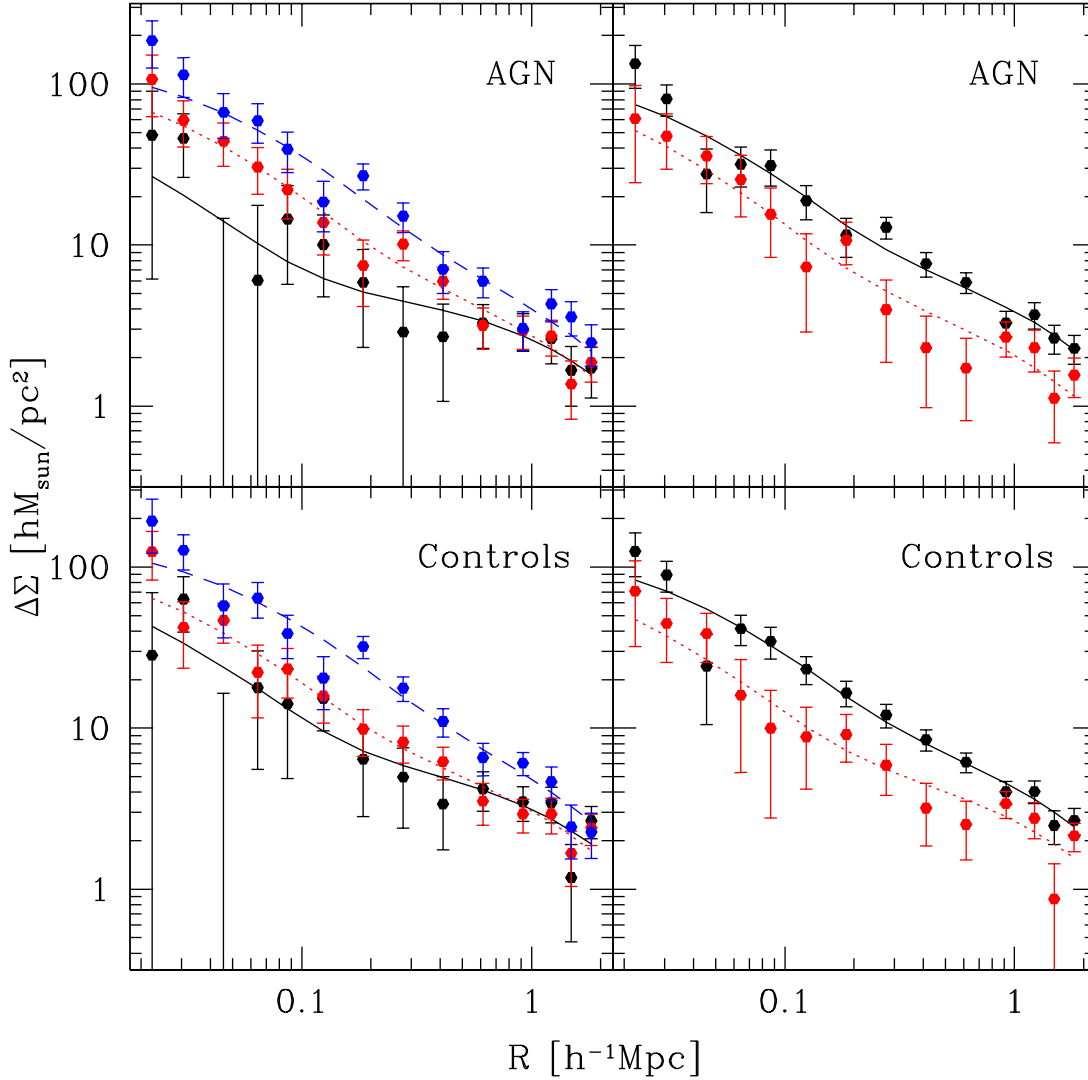Lensing signal for optical AGN and controls

Figure 1. The galaxy-galaxy lensing signal for optical AGN (top) and control galaxies (bottom) as a function of transverse separation. Points are the data, and lines are the best-fitting halo models. The left panels show the sample split by stellar mass as follows: $\log M_* < 10.6$ (black solid), $10.6 \leqslant \log M_* < 11$ (red dotted), $\log M_* \geqslant 11$ (blue dashed). The right panels show the sample split by $L[\text{OIII}]/M_{bh}$ into the lower half of the sample (black solid) and upper half (red dotted).

The lensing signal is presented in comoving coordinates, with angular diameter distances computed assuming a flat ΛCDM universe with $\Omega_m = 0.3$ and $\Omega_\Lambda = 0.7$. The halo model used to interpret the lensing signal assumes $\sigma_8 = 0.9$. In the units used, H_0 scales out of everything, so our results are independent of this quantity. The central halo mass definition for this paper is the mass within which the spherical overdensity is $200\rho_{crit}$, which is roughly 35 per cent lower than the mass definition used for previous lensing analyses using this halo model formalism (Mandelbaum et al. 2005b, 2006). This change in halo mass definition was made to match the mass definition for the clustering analysis.

3.4 Clustering analysis

3.4.1 The reference galaxy sample

In this paper, the clustering of AGN (or control galaxies) is quantified by the projected two-point cross-correlation function (2PCCF), $w_p(r_p)$, which is estimated by cross-correlating the AGN (or control) samples described above with a reference sample of galaxies.[2] The reference galaxies are selected from `sample dr4` of the New York University Value Added Galaxy Catalogue (NYU-VAGC), which is based on SDSS DR4, publicly available at

---

[2] We use the notation r_p for the transverse separation in the clustering analysis, and the notation R for the same quantity in the lensing analysis. The main reason is to maintain notational consistency within previous work.

http://sdss.physics.nyu.edu/vagc/, and is described in detail in Blanton et al. (2005). The reference sample contains 292,782 objects that are identified as galaxies from the Main sample and have $0.01 \leqslant z \leqslant 0.3$, $14.5 < r < 17.6$ and $-23 < M_{0.1_r} < -17$. This sample has formed the basis of our recent investigations of the clustering properties of different classes of galaxies (L06, Li et al. 2007a, 2008a,b).

3.4.2 *Clustering measures*

Our methodology for computing correlation functions has also been described in detail in our previous papers. Random samples are constructed with the same selection function as the reference sample, as described in detail in Li et al. (2006a) (but note the slight differences mentioned here in §3.2.1). The redshift-space 2PCCF $\xi(r_p, \pi)$ between AGN (or control galaxies) and the reference sample is then calculated using the estimator presented in L06,

$$\xi(r_p, \pi) = \frac{N_R}{N_D} \frac{QD(r_p, \pi)}{QR(r_p, \pi)} - 1, \tag{8}$$

where r_p and π are the separations perpendicular and parallel to the line of sight; N_D and N_R are the number of galaxies in the reference sample and in the random sample, with $N_R/N_D = 10$ throughout this paper; $QD(r_p, \pi)$ and $QR(r_p, \pi)$ are the cross pair counts between AGN/control and the reference sample, and between AGN/control and the random sample, respectively. Finally, the redshift-space projected 2PCCF $w_p(r_p)$ is estimated by integrating $\xi(r_p, \pi)$ along the line-of-sight direction:

$$w_p(r_p) = \int_{-\pi_{max}}^{+\pi_{max}} \xi(r_p, \pi) d\pi = \sum_i \xi(r_p, \pi_i) \Delta \pi_i. \tag{9}$$

Here $\pi_{max} = 40h^{-1}$ Mpc, and the summation for computing $w_p(r_p)$ runs from $\pi_1 = -39.5$ h^{-1} Mpc to $\pi_{80} = 39.5$ h^{-1} Mpc, with $\Delta \pi_i = 1$ h^{-1} Mpc. We have also corrected carefully for the effect of fibre collisions; a description and tests of the method can be found in L06. As will be described in more detail in § 4.2.1, error estimates come from the variance in $w_p(r_p)$ between 100 mock catalogues.

The clustering computation assumes the same flat ΛCDM universe with $\Omega_m = 0.3$, $\Omega_\Lambda = 0.7$ and $\sigma_8 = 0.9$ as for the lensing analysis. Our results are presented in units of h^{-1} Mpc with $h = 1$.

4 RESULTS

4.1 Optical AGN

Results and interpretation for the galaxy clustering signal of the optical AGN have been presented in L06, and are also briefly described in §2.2. Consequently, here we present only the galaxy-galaxy lensing signal and its interpretation for this sample. In section 5, we compare the halo masses and satellite fractions estimated through lensing with the same quantities estimated through clustering.

In Fig. 1, we show the g-g lensing signal for the optical AGN sample split by stellar mass and by the accretion rate per unit black hole mass ($L[OIII]/M_{bh}$). Results are shown for both the AGN and the control samples; results for the control samples with the same distribution of D_{4000} are not
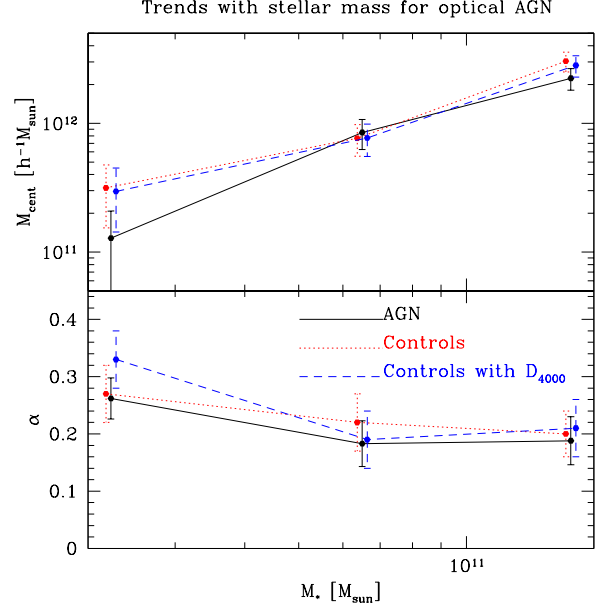

Figure 2. The best-fitting central halo masses M_{cent} (top) and satellite fractions α (bottom) as a function of stellar mass for the optical AGN and the two control samples as labelled on the plot.

shown, because they are statistically consistent with the results for the control samples where D_{4000} is not matched.

There are several clear trends in this figure. First, the g-g lensing signal on small scales ($< 0.3h^{-1}$Mpc) shows that the halo mass for central galaxies increases with stellar mass and decreases with $L[OIII]/M_{bh}$. This conclusion is true for both the AGN and for the control samples. Second, the g-g lensing signal for AGN and controls in a particular subsample is quite similar; any differences are not statistically significant.

We now consider the halo model interpretation of these results, represented by the best-fitting central halo mass and satellite fraction for each sample. These quantities are plotted for the optical AGN and the two control samples in Fig. 2 as a function of stellar mass. For reference, they are tabulated for all optical AGN and control subsamples, including the splits by $L[OIII]/M_{bh}$, in Table 1.

A few trends are evident from the plot and table. First, for the samples split by stellar mass, the differences in halo model parameters for the AGN and control samples are not statistically significant, as expected from Fig. 1. However, the central halo mass shows a strong trend with stellar mass, consistent with the lensing results for the general galaxy population discussed in Mandelbaum et al. (2006). If we compare against the results in that paper after accounting for the different halo mass definitions, we conclude that for the lower and middle stellar mass bins, the best-fitting central halo mass is consistent (within the noise) with the results for both early and late type galaxies, which have similar mean halo masses below stellar masses $\sim 10^{11} M_\odot$. For the highest stellar mass bin, our best-fitting central halo mass is more consistent with the results for late-type galaxies (lower by a factor of a few than that for early-type galaxies). This result is consistent with the general tendency of these narrow-line AGN to be associated with galaxies with ongoing star formation.

Table 1. Best-fitting halo model parameters for fits to the optical AGN g-g weak lensing signal, with 68 per cent CL errors.

Sample	Optical AGN		Controls		Controls with D_{4000}	
	M_{cent} $10^{12}h^{-1}M_{\odot}$	α	M_{cent} $10^{12}h^{-1}M_{\odot}$	α	M_{cent} $10^{12}h^{-1}M_{\odot}$	α
$\log M_*/M_{\odot} < 10.6$, $\langle M_*/(10^{10}M_{\odot})\rangle = 2.3$	0.13 ± 0.08	0.26 ± 0.04	0.31 ± 0.16	0.27 ± 0.05	0.29 ± 0.15	0.33 ± 0.05
$10.6 \leqslant \log M_*/M_{\odot} < 11$, $\langle M_*/(10^{10}M_{\odot})\rangle = 6.5$	0.86 ± 0.21	0.18 ± 0.04	0.77 ± 0.20	0.22 ± 0.05	0.79 ± 0.21	0.19 ± 0.05
$\log M_*/M_{\odot} \geqslant 11$, $\langle M_*/(10^{10}M_{\odot})\rangle = 15.4$	2.3 ± 0.4	0.19 ± 0.04	3.0 ± 0.5	0.20 ± 0.04	2.8 ± 0.6	0.21 ± 0.05
Lower half, $L[OIII]/M_{bh}$	1.1 ± 0.2	0.25 ± 0.03	1.5 ± 0.2	0.25 ± 0.03	1.1 ± 0.2	0.30 ± 0.03
Upper half, $L[OIII]/M_{bh}$	0.47 ± 0.13	0.16 ± 0.03	0.39 ± 0.14	0.22 ± 0.03	0.52 ± 0.16	0.17 ± 0.03
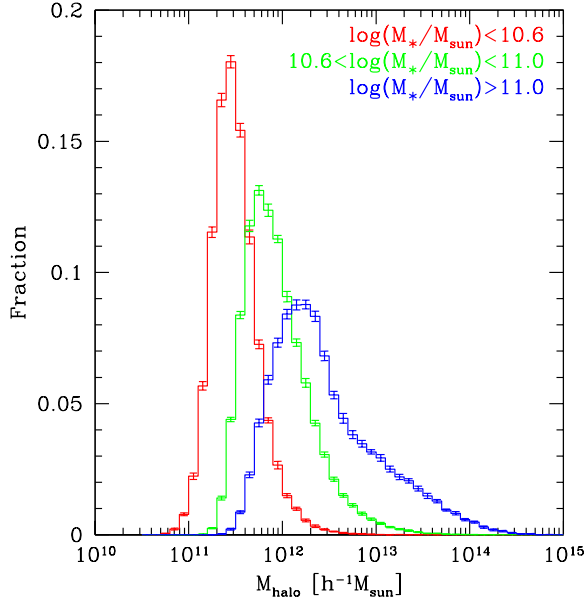
Figure 3. The distributions of central halo mass in the mock catalogues that are able to reproduce the clustering signal in Li et al. (2006b) in our three stellar mass bins.

The satellite fractions decrease slightly from the lowest to middle stellar mass bin. Consistent with the results from L06, we find slightly lower satellite fractions for the optical AGN than for the control samples. Unlike for the galaxy clustering signal, this difference is not statistically significant.

There is clearly a significant difference in the mean central halo mass and satellite fraction for the samples split at the median value of $L[OIII]/M_{bh}$. However, this quantity is itself correlated with stellar mass, so some of the trend derives from that correlation. For the lower half of the sample in OIII luminosity, the mean stellar mass is $\langle M_*\rangle = 9.1 \times 10^{10}M_{\odot}$; for the upper half, it is $7.3 \times 10^{10}M_{\odot}$. The results for the control samples with the same stellar mass distribution suggest that the difference in best-fitting central halo masses can be explained solely by this difference in stellar mass distributions.

Finally, we discuss the broadness of the central halo mass distribution. As we have already noted, a broad central halo mass distribution would lead to the best-fitting central halo masses being an overestimate of the median mass, and underestimate of the mean mass. To assess whether this may be the case, we use the halo occupation models of L06 for optical AGN (see §2.2) which can be used to derive a cen-

tral halo mass distribution. This plot is shown in Fig. 3. As shown, the FWHM of the distribution for the two lower stellar mass bins is within the factor of ~ 6 needed for accurate estimation of the mean central halo mass. However, the distribution is sufficiently broad for the highest stellar mass bin that our estimate from the lensing signal is likely an underestimate of the mean, possibly by as much as 50 per cent. We do not apply a correction to determine the mean central halo mass for either the AGN or the controls in this bin, since there is significant systematic uncertainty in the correction factor itself.

4.2 Radio AGN

4.2.1 Galaxy Clustering

We have measured the projected 2PCCF $w_p(r_p)$ of the radio AGN with respect to the reference galaxies, and compared this to the average result of the five control samples. The results are shown in Fig. 4 for the whole sample (circles in the left panel) and for two different ranges in stellar mass M_*.

Radio AGN are more strongly clustered than control galaxies on all scales. The difference in $w_p(r_p)$ amplitude is a constant factor on scales smaller than ~ 1 Mpc, then rises slightly on larger scales. Fig. 4 also shows that the clustering amplitude of radio AGN increases with the stellar mass of the host galaxy. This result is consistent with the fact that more massive galaxies are more strongly clustered (Li et al. 2006a). We have also tested whether there is a dependence of the clustering amplitude on the radio luminosity of the AGN, and we find that at fixed M_*, there is no significant effect. This finding is consistent with the recent results of Kauffmann et al. (2008), who show that radio-loud AGN are in denser environments than control radio-quiet galaxies, but that there is no dependence of local density on the radio luminosity of the AGN.

We now use our mock catalogues (see §3) to model the observed clustering measurements of radio AGN. We first tried to vary the fraction of radio AGN assigned to central versus satellite galaxies (as was done for the optical AGN). We found that if radio AGN are preferentially found in satellite galaxies, we can fit the data on scales smaller than a few Mpc, but the model then underpredicts the clustering amplitude on larger scales. As we have discussed, the amplitude of the correlation function on scales larger than a few Mpc provides a direct measure of the mass of the dark matter halos hosting the radio AGN. Motivated by the models of Croton et al. (2006) and Bower et al. (2006), we impose a lower threshold in halo mass, M_h^{min}, as a second free pa-
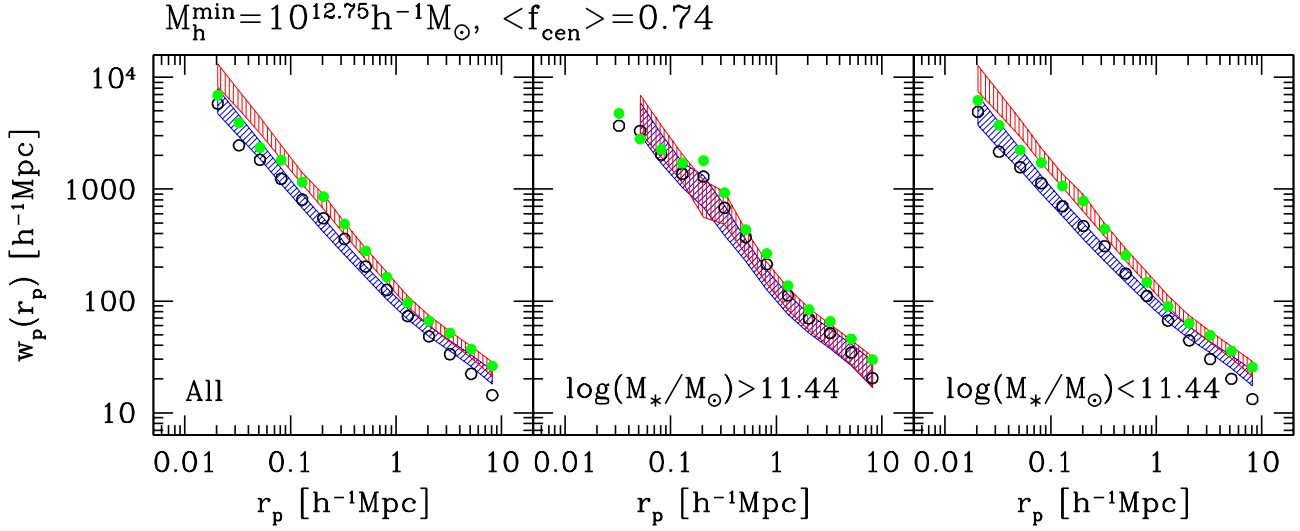
Figure 4. Projected cross-correlation function $w_p(r_p)$ for radio AGN (green filled circles) in different stellar mass ranges compared to results for control samples selected without regard to AGN properties (black open symbols). Results for the best-fitting model are indicated as red (AGN) and blue (controls) shaded regions, where the width of the shaded regions corresponds to the $1 - \sigma$ variance between 200 mock catalogues. Errorbars are significantly correlated (> 10 per cent) between radial bins above $\sim 1h^{-1}$Mpc.

rameter of the model. In other words, radio-loud AGN are only found in dark matter halos more massive than M_h^{min}. The probability of a galaxy to be a radio-loud AGN depends not only on whether it is a central or satellite system, but also on the mass of its dark matter halo. However, the probability that a particular galaxy is an AGN does not depend on the AGN status of its neighbors. While this step function in mass is undoubtedly an over-simplification, we adopt it as a first attempt at modeling to see if it is close enough to reality that the observations can be modeled in this way.

We have generated a grid of 322 models by varying the two parameters, f_{cen} and M_h^{min}, with f_{cen} ranging from 0.40 to 0.84 with a step size of 0.02, and $\log(M_h^{min}/h^{-1}M_\odot)$ ranging from 10.0 to 13.25 with a step size of 0.25. We have constructed 200 mock catalogues of radio AGN for each of the models. We measure $w_p(r_p)$ and its covariance matrix $\mathbf{C}$ at each grid point, and we compare the measurements to the SDSS results. In order to identify the best-fit model, we first calculate the likelihood of each parameter set, $L(f_{cen}, M_h^{min})$, by

$$L(f_{cen}, M_h^{min}) = \frac{(2\pi)^{-m/2}}{\det[\mathbf{C}(f_{cen}, M_h^{min})]} e^{-0.5\chi^2(f_{cen}, M_h^{min})}, (10)$$

where

$$\chi^2(f_{cen}, M_h^{min}) = \mathbf{X}^T \mathbf{C}^{-1} \mathbf{X}. \tag{11}$$

Here $\mathbf{X} = \{X_j\}$ $(j = 1, ..., m)$ is an $m \times 1$ vector with

$$X_j = \left(\frac{1}{n} \sum_{i=1}^{n} w_{p,i}(r_{p,j})_{model} \right) - w_p(r_{p,j})_{SDSS}, \tag{12}$$

where $n = 200$ is the number of mock catalogues, m is the number of radial bins over which $w_p(r_p)$ is measured, $w_p(r_{p,j})_{SDSS}$ is the clustering amplitude at the jth radial bin as measured from the SDSS, and $w_{p,i}(r_{p,j})_{model}$ is the result at the jth radial bin as measured with the ith mock

catalogue. The $m \times m$ matrix $\mathbf{C} = \{C_{ij}\}$ $(i, j = 1, ..., m)$ is the covariance matrix of the measurements from the 200 mock catalogues, given by

$$C_{i,j} = \frac{1}{n-1} \left[\sum_{k=1}^{n} (Y_{ki} - \langle Y_i \rangle)(Y_{kj} - \langle Y_j \rangle) \right] \tag{13}$$

where

$$Y_{k,i} = w_{p,k}(r_{p,i})_{model} \tag{14}$$

is the measurement at the ith radial bin from the kth mock catalogue, and

$$\langle Y_i \rangle = \frac{1}{n} \sum_{k=1}^{n} w_{p,k}(r_{p,i})_{model} \tag{15}$$

is the mean measurement at the ith radial bin over all mock catalogues.

We define the best-fit model to be the one giving a minimum Λ computed as follows:

$$\Lambda(f_{cen}, M_h^{min}) = -2 \ln L(f_{cen}, M_h^{min}) \tag{16}$$
$$= \chi^2(f_{cen}, M_h^{min}) + 2\ln\{\det[\mathbf{C}(f_{cen}, M_h^{min})]\} + m\ln(2\pi).$$

Note that this maximum likelihood estimate differs from the simple minimum of χ^2 if the determinant of the covariance matrix $\det[\mathbf{C}]$ varies with the parameters. This variation is demonstrated in Figure 5, where we plot $\ln[\det(\mathbf{C})]$ in the grid of the two model parameters, f_{cen} and M_h^{min}. As can be seen, the determinant of the covariance matrix does vary systematically from model to model. This variation is due to the fact that the covariance depends on the two- and four-point functions of the galaxy distributions, which clearly differ across the grid due to the different ways the halos are populated with AGN. However, the variation is relatively smooth, indicating that we have used enough mock catalogues at each grid point (200) to determine the covariance matrix with a sufficiently small noise level.
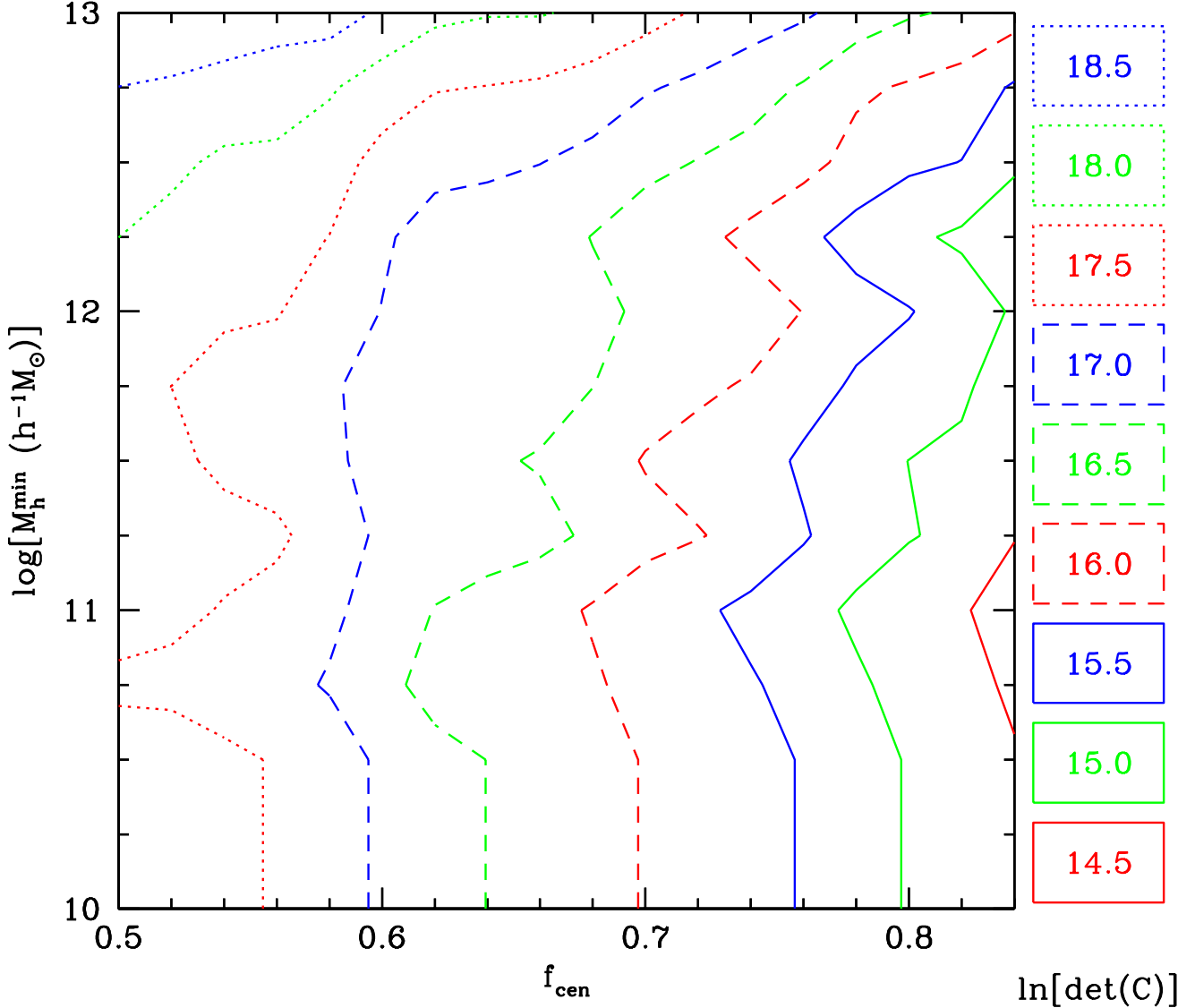
Figure 5. Determinant of the covariance matrix of $w_p(r_p)$ (see Eq. 13), on the grid of the two model parameters, f_{cen} and M_h^{min}. f_{cen} is the fraction of radio AGN that are hosted by the central galaxy of their own dark matter halo, and M_h^{min} is the minimum mass for the halos that can host radio AGN. The contour levels are indicated at the right-hand side.

We compare the measured $w_p(r_p)$ with the models in four radial bins centered at $r_p = 0.21$, 0.65, 2.1 and 6.5 h^{-1}Mpc, with a step size of $\Delta \log r_p = 0.5$ (larger than the radial bins shown in the plots). The choice of 4 radial bins was motivated by tests showing that the covariance matrices evaluated from the mock catalogues were well-behaved in this case, whereas using a significantly larger number of radial bins causes the covariance matrices (a) to be noisier, and (b) to have peculiar patterns of correlations between bins suggestive of edge effects (in particular, strong correlations between certain adjacent pairs of radial bins that are not representative of the overall pattern of correlations). These particular radial bins were chosen to sample separate parts of the HOD, namely the central 1-halo term, the satellite 1-halo term, the transition between the 1- and 2-halo terms, and the 2-halo term (respectively). The minimum ra-

dius was chosen because the data at smaller separations are rather noisy.

Fig. 6 plots the contours of $\Delta \Lambda = \Lambda - \Lambda_{min}$ in the grid of the two parameters, when using the $w_p(r_p)$ measurements for the full radio-loud AGN sample (left panel of Fig. 4). The $1, 2,$ and 3σ confidence regions, computed for $m = 4$ and 2 parameters, are indicated using solid, dashed and dotted black lines. We have explicitly checked the distribution of χ^2 values for the individual mock catalogs to ascertain that the Gaussian approximation for the likelihood is valid, and found that the cumulative distribution of χ^2 matches the expected distribution at extremely high confidence (using the Kolmogorov-Smirnov test) at all points on the grid. Consequently, the method we have used to determine confidence regions is valid. The minimum Λ_{min}, appears at $f_{cen} = 0.74$

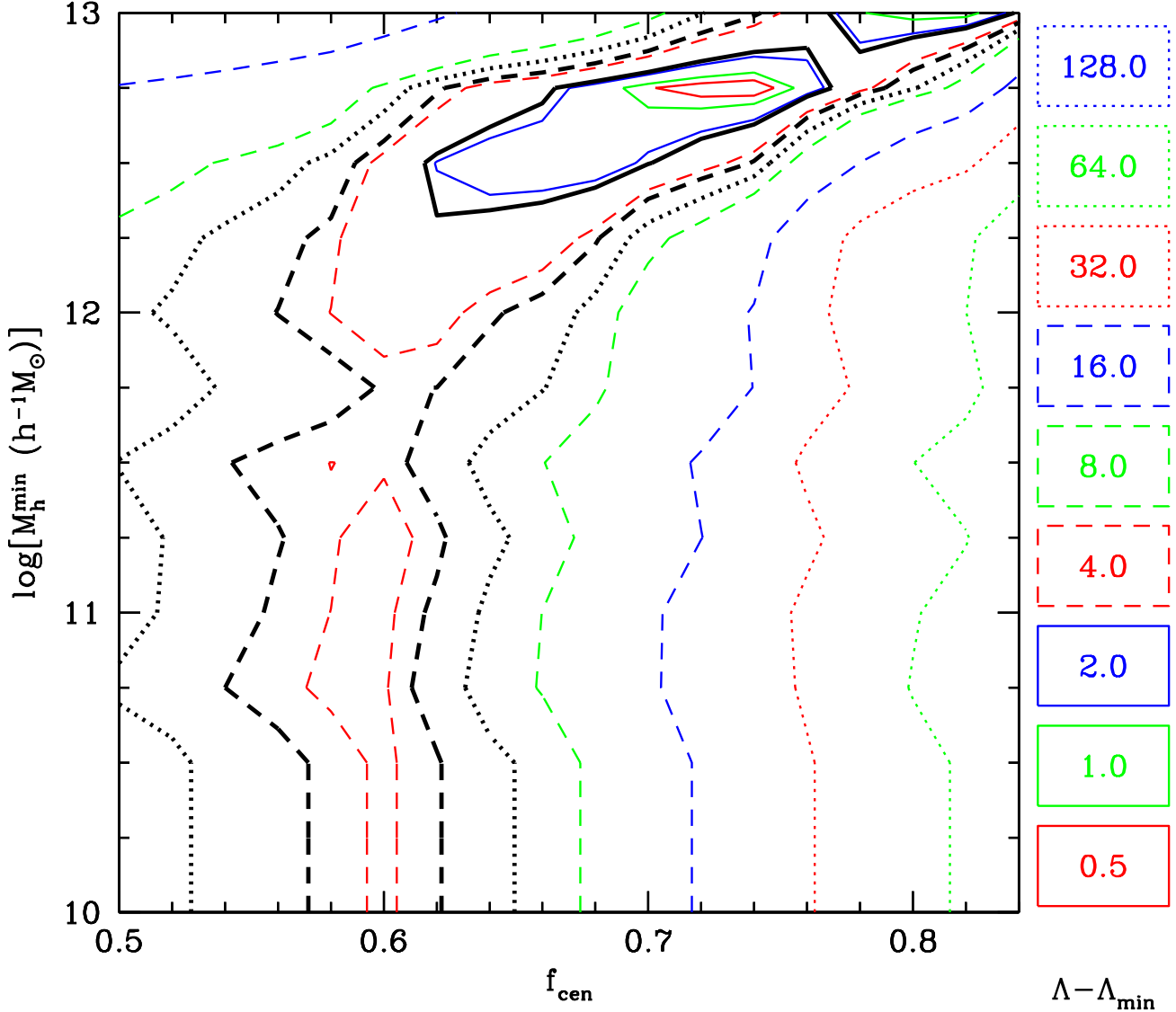**Figure 6.** Λ, defined by Eq.(16) and derived by comparing the projected 2PCCF $w_p(r_p)$ for the whole sample of radio AGN as predicted by the halo occupation model and as measured from the SDSS data, is plotted with respect to the minimum value Λ_{min}, in the grid of the two model parameters, f_{cen} and M_h^{min}. The contour levels, as indicated at the right-hand side, are chosen to cover the full range of Λ produced by all the models. The 68.3%, 90% and 95.4% confidence levels are plotted as solid, dashed and dotted black lines.

and $M_h^{min} = 10^{12.75} h^{-1} M_\odot$ with $\chi^2/d.o.f. = 0.5$, indicating that the fit is acceptable.

However, there is a strong degeneracy between the two parameters in the sense that models with smaller f_{cen} and lower M_h^{min} can also provide a reasonable fit to the data. While this minimum is the preferred solution at the 1-σ level, there is a banana-shaped degeneracy region extending down to $(0.60, 10.0)$ that is allowed at the 2-σ level. The slight saddlepoint at $(0.60, 11.75)$ that appears to divide this region does not have a sufficiently large $\Delta\Lambda$ relative to the minimum that we can robustly consider it is being real. As shown in Fig. 7, the residual noise in Λ due to the use of finite N_{mock} for the modeling is comparable to the size of $\Delta\Lambda$ that creates this apparent saddlepoint. The noise in Λ was determined by bootstrapping the (roughly independent) N_{mock} to make many new sets of mock catalogs and de-

termining the variance between Λ for these sets of N_{mock}. However, the size of $\Delta\Lambda$ that distinguishes this degeneracy region from the rest of the plane in (f_{cen}, M_h^{min}) is significantly larger than the noise in Λ. The reason that we are able to fit the data reasonably well at other points in this degeneracy region, despite the very different halo model parameters, is that the higher satellite fraction places more AGN as satellites in very massive halos, offsetting the lower bias for central AGN due to the lower M_h^{min}.

We now use the center and right panels of Fig. 4 to evaluate whether the model that best fits the data for the full sample can also describe the data for the sample split into two stellar mass bins. We have repeated the above analysis with two samples of radio AGN with $\log M_* < 11.44$ and $\log M_* \geqslant 11.44$. We evaluate the correlation function using the same radial bins for 200 mock catalogues. We see that
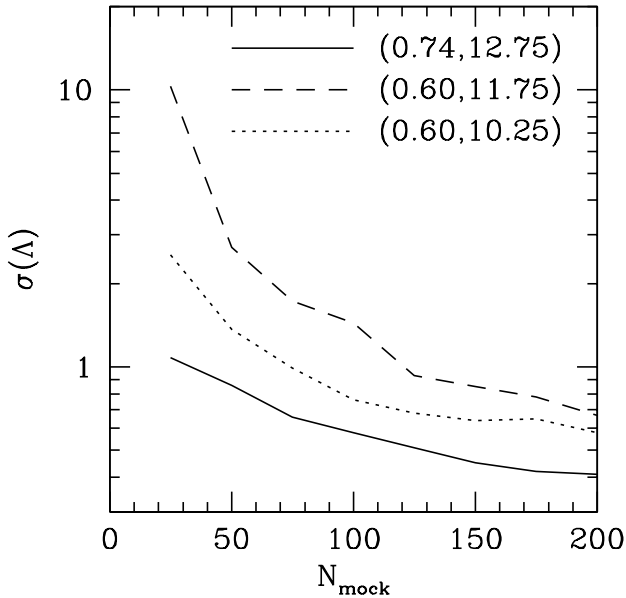
Figure 7. Noise in contour plot of Λ, Figure 6, due to finite N_{mock}, as determined from bootstrap resampling of the 200 mock catalogs. The noise as a function of N_{mock} is shown for three different points on the grid: the global minimum, and two other points in the degeneracy region.

while the model is able to describe the data for the lower stellar mass bin quite well, including the significant separation in signal between radio AGN and controls, there is some tension between the observations and the model for the higher stellar mass bin. As shown, the observed signals still have a significant offset, but the model signals are nearly the same for the radio AGN and for the controls. This is not surprising, since at these high stellar masses, essentially all halos are above M_h^{min}. Consequently, the apparent failure of the model at high stellar mass most likely results from the fact that a step-function model for the radio AGN probability is overly simplistic. A probability that is a function of mass would allow for a better description, but unfortunately the data quality do not justify adding additional halo model parameters at this time, so we defer such an analysis to future work with more data.

4.2.2 Galaxy-galaxy lensing

Here we present the galaxy-galaxy weak lensing signal for the radio-loud AGN sample, along with the halo model fits. These results are shown in Fig. 8 for the full radio-loud AGN and control samples (upper left); a stellar mass subsample containing the lower 2/3 of the sample in stellar mass (lower left); the remaining upper 1/3 of the sample in stellar mass (upper right); and the radio-loud AGN split by $\log{(P/M_{bh})}$ (lower right).

A number of trends are evident in Fig. 8. First, we see that the lensing signal is higher on all scales ($R < 2h^{-1}\mathrm{Mpc}$) for the radio-loud AGN than for the control sample. Second, this trend persists in the different stellar mass subsamples. Third, the lensing signal increases with stellar mass, as expected. Finally, the lensing signal for the two bins in

$\log{(P/M_{bh})}$ are not markedly different from each other. For the lower and higher bins in this quantity, the mean stellar masses are 2.45 and $2.75 \times 10^{11} M_\odot$, respectively, a difference of only 10 per cent, much less than the difference between the mean stellar masses for the two stellar mass bins, so this near equivalence is not surprising.

Next, we present the halo model interpretation of these results. Table 2 gives the best-fitting halo model parameters for each of the subsamples shown in Fig. 8. We focus on the results for central halo masses, because the satellite fractions are quite noisy. For the full sample, the best-fitting central halo mass M_{cent} is 80 per cent higher for the radio-loud AGN than for the control sample at fixed stellar mass and redshift. When accounting for statistical correlations between the two samples using the bootstrap method, we find that the central radio-loud AGN have higher mass than the controls at the 97 per cent confidence level. For the lower stellar mass bin, this conclusion is less statistically significant (50 per cent higher mass, with $p(M_{cent}^{(AGN)} > M_{cent}^{(controls)}) = 0.71$) but for the higher stellar mass bin, it is more significant than for the full sample (factor of two higher mass, with $p(M_{cent}^{(AGN)} > M_{cent}^{(controls)}) = 0.99$). This result is in sharp contrast to the results for central optical AGN, which appear to have the same halo mass as the optical control galaxies.

When comparing the amplitude of the central halo masses to those for the general galaxy population studied via lensing in Mandelbaum et al. (2006), we find that the results for the control sample are consistent with that paper once we account for the different halo mass definitions, *provided* that we compare to the early type galaxy sample (which has higher mean central halo mass than the late type sample for $M_* > 10^{11} M_\odot$).

Given the high mean halo mass inferred for central radio-loud AGN, we must check our modeling assumption that the range of halo masses is narrow. Fig. 9 shows a plot of the halo mass distribution for model B described in section 4.2.1 which is able to reproduce the radio AGN clustering results. As discussed, this HOD includes a minimum halo mass cutoff of $10^{12.5} h^{-1} M_\odot$. As can be seen, the central halo mass distributions are indeed broader than the factor of ~ 6 that we need for the M_{cent} derived from lensing to be physically meaningful. As before, we do not apply a correction factor, due to the uncertainty in determining it. We merely note that since the AGN are more likely than the controls to reside in clusters (a claim that we will back up via direct comparison with a cluster catalogue), the correction factor to get the mean central halo mass should be *higher* for the AGN than for the controls. Thus, the size of the central halo mass difference between radio-loud AGN and control galaxies is in fact underestimated by our neglect of these corrections.

To avoid uncertainties in the best-fitting halo masses caused by the cluster membership of some galaxies, we have cross-correlated our radio-loud AGN and control samples with a pre-existing SDSS sample of galaxy clusters. We can then compare halo masses for radio-loud AGN and control galaxies in the field (i.e. excluding cluster members). For this sample, the distribution of halo masses will no longer have a tail extending to very high masses.

Since the radio-loud AGN sample is predominantly (85 per cent) in the redshift range $0.1 < z < 0.3$, the natural
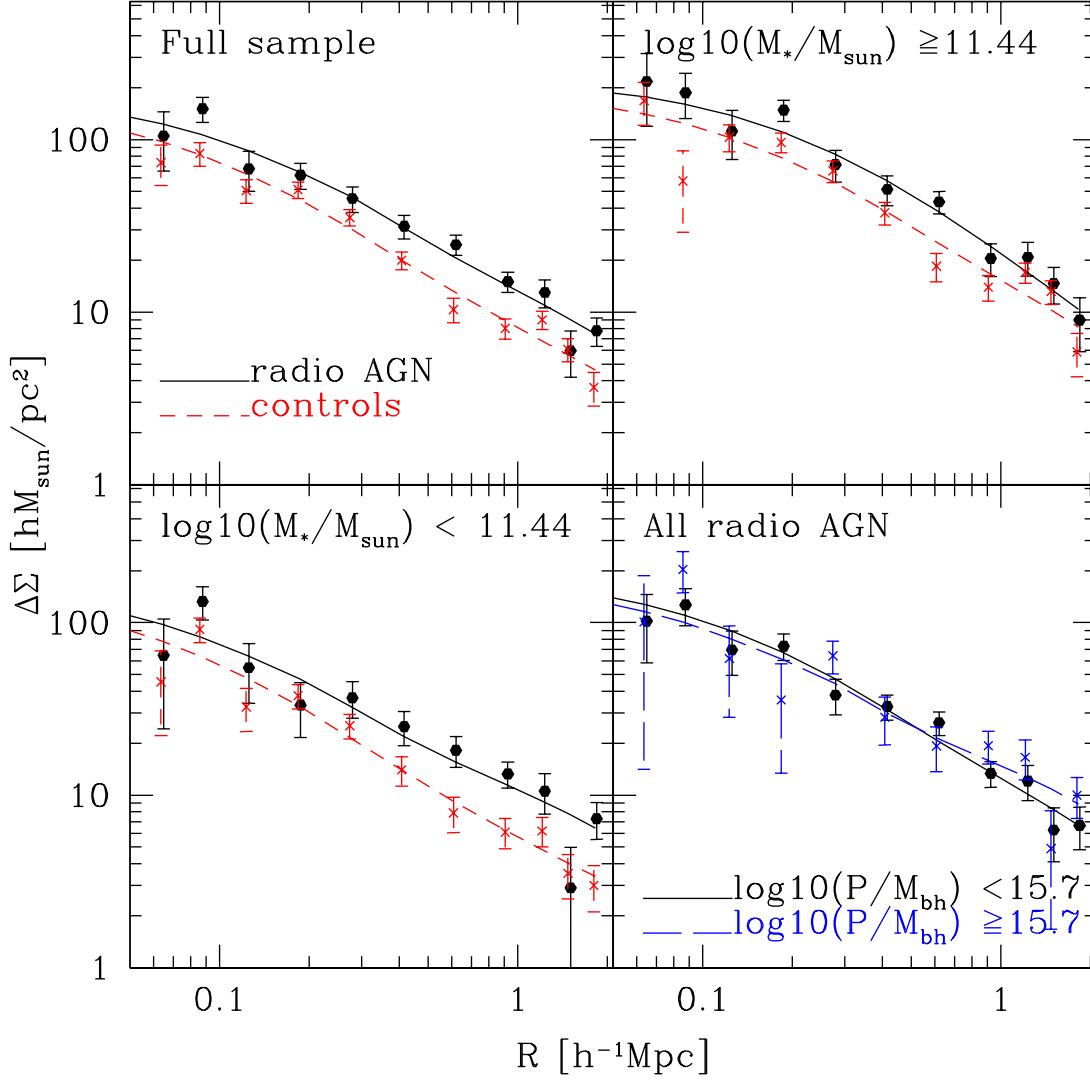
Figure 8. The galaxy-galaxy lensing signal for the radio-loud AGN and control galaxies split into subsamples as indicated on the plot. Points show the measured signal and lines show the best-fitting halo model.

Table 2. Best-fitting halo model parameters for fits to the radio-loud AGN g-g weak lensing signal, with 68 per cent CL errors (in each case, marginalized over the other HOD parameter).

| Sample | Radio-Loud AGN | | Controls | | |
	M_{cent} $[10^{13}h^{-1}M_{\odot}]$	α	M_{cent} $[10^{13}h^{-1}M_{\odot}]$	α	$p(M_{cent}^{(AGN)} > M_{cent}^{(control)})$
Full	1.6 ± 0.4	0.22 ± 0.11	$0.91^{+0.12}_{-0.10}$	0.13 ± 0.05	0.97
$\log(M_*/M_{\odot}) < 11.44$	$0.8^{+0.4}_{-0.5}$	$0.31^{+0.30}_{-0.16}$	$0.56^{+0.11}_{-0.09}$	$0.10^{+0.05}_{-0.07}$	0.71
$\log(M_*/M_{\odot}) \geqslant 11.44$	$4.9^{+0.7}_{-0.9}$	$0.01^{+0.15}_{-0.01}$	2.5 ± 0.4	0.16 ± 0.10	0.99
$\log(P/M_{bh}) < 15.7$	1.8 ± 0.4	$0.13^{+0.15}_{-0.13}$	-	-	-
$\log(P/M_{bh}) \geqslant 15.7$	$1.4^{+0.4}_{-0.9}$	$0.40^{+0.40}_{-0.15}$	-	-	-
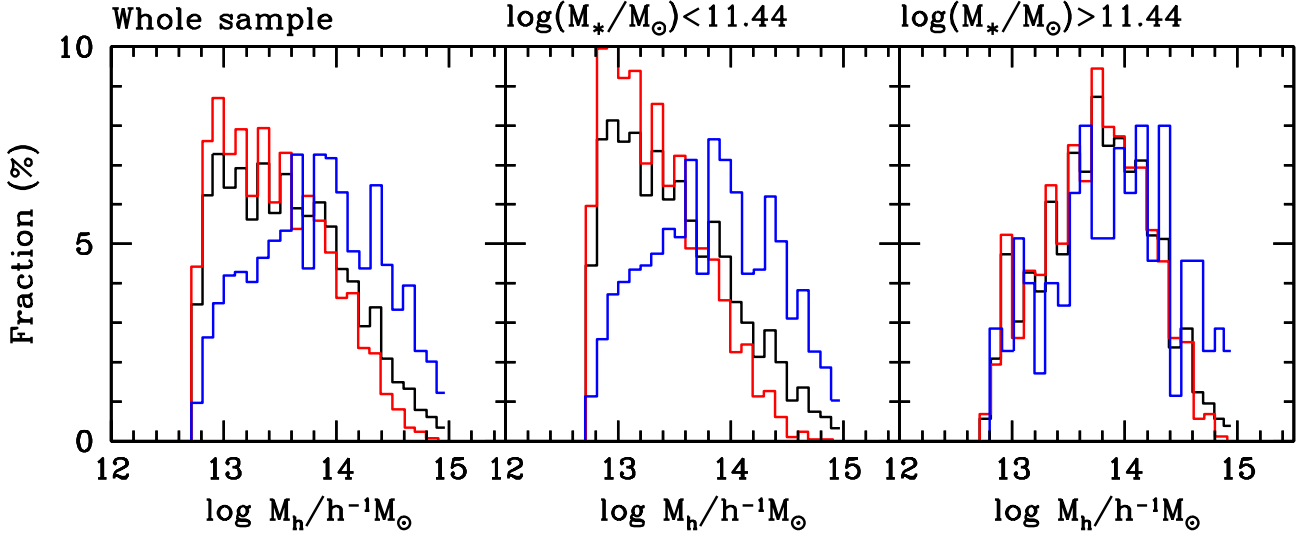
Figure 9. The distributions of halo mass in the mock catalogues that are able to reproduce the clustering signal for radio-loud AGN in the full sample and our two stellar mass bins. Results are shown for the full sample (black lines), central galaxies only (red lines), and satellites only (blue lines).

choice of cluster catalogue is the SDSS MaxBCG catalogue (Koester et al. 2007b,a), which contains clusters in the redshift range $0.1 < z < 0.3$ that are selected based on the existence of a red sequence.

We select radio-loud AGN and control galaxies in this redshift range and check whether they are within $1h^{-1}$Mpc (physical projected separation) of a cluster, and within $\Delta z = \pm 0.04$ of the cluster BCG. We note that the choice of redshift separation is a factor of ten larger than the velocity dispersion of even the very largest galaxy clusters. The motivation for this choice comes from the typical photometric redshift error of the galaxies in the maxBCG catalogue, and ensures that 95 per cent of true cluster members would be found. For reference, the minimum mass of the public maxBCG catalogue, with scaled richness $\geqslant 10$, is $\sim 6 \times 10^{13} h^{-1} M_{sun}$ (defined using $M_{200\overline{\rho}}$, Reyes et al. 2008). We also determined whether the radio-loud AGN or control is the cluster BCG or a satellite. These statistics are presented for radio-loud AGN and controls for both the full sample and for subsamples selected according to stellar mass in Table 3.

The numbers presented there for each sample are defined as follows:

$$f_{\text{clust}} = \frac{\text{Number in sample that are in a cluster}}{\text{Number in sample}} \quad (17)$$

and

$$f_{\text{BCG}} = \frac{\text{Number in sample that are BCG of a cluster}}{\text{Number in sample}} \quad (18)$$

Based on this table, we note a few interesting trends. First, for all subsamples we considered, f_{clust} and f_{BCG} are higher for the radio-loud AGN than for the controls. This difference is most pronounced for the lower stellar mass bin, with a factor of two difference between radio-loud AGN and controls. For the higher stellar mass bin, the differences are at the ~ 20 per cent level. These results are broadly in agreement with those of Best et al. (2007).

Second, if we compare these two numbers for a given sample, we can determine the fraction of those *in clusters* that are BCGs, where the rest are satellites. For the full radio-loud AGN and the control samples, this number is 60 per cent. Thus, on average, the distribution of centrals versus satellites for those that are cluster members is the same for radio-loud AGN and control galaxies. For the lower and higher stellar mass samples, we again find consistency between the radio-loud AGN and controls, with BCG fractions of those that are in clusters of 40 per cent and 85 per cent, respectively.

It is apparent that the halo mass distributions of both the radio-loud AGN and control samples may have significant contributions from cluster BCG and satellite galaxies, which will skew the halo mass distribution to the high mass end. Consequently, we repeat the weak lensing analysis using only those galaxies in the redshift range $0.1 < z < 0.3$ that are not within any maxBCG cluster. This cuts down the size of the sample significantly at the high stellar mass end, so we only analyze the full sample, without any divisions in stellar mass or radio power.

The lensing signal for these "field samples" is shown in Fig. 10, along with the best-fitting halo model. We initially used the same halo model as before, but found that the satellite fractions were all consistent with zero within the noise (as one would expect given the sample design). Thus, we redid the fits with fixed $\alpha = 0$, fitting for central halo mass only.

The mean stellar mass for these field samples is $2.1 \times 10^{11} M_{\odot}$. The reduction in best-fitting central halo mass going from the full radio-loud AGN and control samples, to the field subsamples, is roughly 15 per cent. This reduction is expected, since we have excluded the AGN in clusters, which have typical halo masses of $> 10^{14} M_{\odot}$. In both cases, however, for the full samples and for the field subsamples, the best-fitting central halo mass for the radio-loud AGN sample is roughly twice that of the control samples. We have

Table 3. Results of matching the radio-loud AGN and control samples with $0.1 < z < 0.3$ against the maxBCG cluster catalogue. Quantities presented in the table are defined in Equations 17 and 18.

Sample	$f_{\rm clust}$ (AGN)	$f_{\rm clust}$ (controls)	$f_{\rm BCG}$ (AGN)	$f_{\rm BCG}$ (controls)
Full	0.24	0.16	0.14	0.09
$\log M_* < 11.44$	0.20	0.12	0.08	0.05
$\log M_* \geqslant 11.44$	0.36	0.29	0.31	0.23
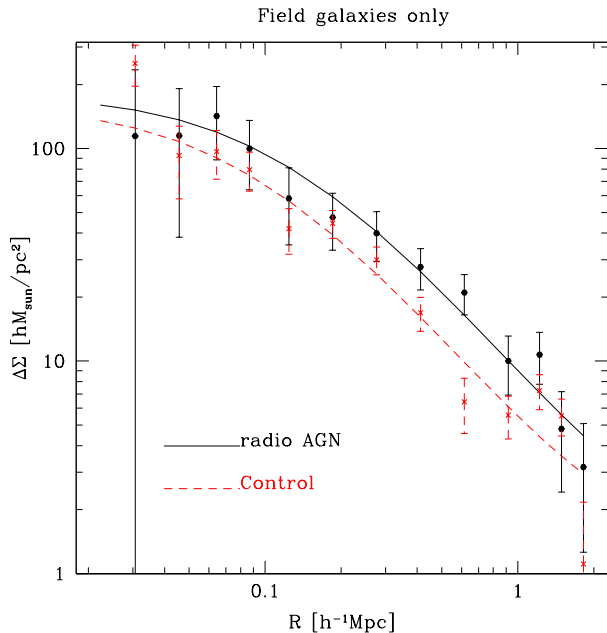
Figure 10. The galaxy-galaxy lensing signal for the radio-loud AGN and control galaxies located in the field with $0.1 < z < 0.3$. Points show the measured signal and lines show the best-fitting halo model.

already explored this result for the full sample; for the field sample, we find best-fitting central halo masses of (1.5 ± 0.3) and $(0.76 \pm 0.14) \times 10^{13} h^{-1} M_\odot$ (radio AGN and controls, respectively). The difference between the two masses is thus significant at the 97 per cent CL.

4.3 Joint constraints on halo masses and satellite fractions of radio AGN

In section 4.2.1, we presented a best-fitting HOD model that well reproduced the clustering signal of radio AGN and the control sample. In this section, we compare the results of the model to the results obtained from the lensing analysis.

In Fig. 11, we plot the mean halo mass of the central radio-loud AGN and the fraction of satellite AGN, as predicted by the best-fitting model describing the clustering results, as a function of stellar mass. The results from the lensing analyses are also plotted. As discussed in the previous section, the lensing analysis finds a higher mean halo mass for radio AGN at slightly more than 2σ, which persists even when radio AGN residing in clusters are excluded from the analysis. This difference is even more significant, at the 99 per cent CL, for the higher mass subsample.

As shown, the model that best describes the clustering results is consistent with the g-g lensing results in the sense

that different mean masses are predicted for the controls and the radio AGN. As already discussed, the fact that the same masses are predicted for the two samples in the higher mass bin is a consequence of overly-simplistic modeling. While the g-g lensing estimates of the satellite fraction are fairly noisy, they are also consistent with the model that describes the clustering. It would be valuable to confirm our conclusions using larger radio AGN samples that will be available in the future. This is particularly true at very low stellar masses ($< 10^{11} M_\odot$), where a measurement with lensing was not at all possible and where we would be most sensitive to the difference between radio AGN and controls. When samples are available with significantly better statistics, the data quality will warrant a more careful analysis using the mocks to compare against both the clustering and lensing signal, and possibly more sophisticated halo modeling than that which was attempted here.

5 SUMMARY

We now present a comparison of the inferred halo masses and satellite fractions of both optical and radio-loud AGN, from both the clustering and g-g lensing techniques.

In the left panel of Fig. 12, we plot the inferred central halo masses of optical AGN (cyan) and radio AGN (green) from the lensing analysis as a function of stellar mass. The solid symbols give results for the AGN, while the open symbols give results for the control samples.

In the middle panel, we plot the inferred central halo masses of optical (blue) and radio AGN (red) from the clustering analysis. The results are from the published model of Li et al. (2006b) for the optical AGN, and the magenta lines show our best-fitting model for the radio AGN presented in section 4.2.1. The halo mass as a function of stellar mass is plotted as solid lines for the AGN and as dashed lines for the control galaxies. As can be seen, the clustering technique allows us to extend the halo mass measurements over a significantly larger range in stellar masses. We have experimented with subsamples with even lower stellar masses and we found that we are able to derive a (noisy) clustering measurement for radio galaxies with stellar masses less than $10^{11} M_\odot$, but there are too few objects to permit a lensing analysis to be carried out. Lensing measurements at lower stellar mass with larger, future datasets may be critical for reducing the modeling uncertainty indicated in this figure. Note that the convergence of the curves at high stellar mass is a consequence of our very simple model which has little or no flexibility to adjust the clustering of high mass stellar mass objects, the great majority of which are central galaxies and live in massive halos.

Finally, in the right-hand panel, we superimpose the clustering and lensing results. We see that the agreement
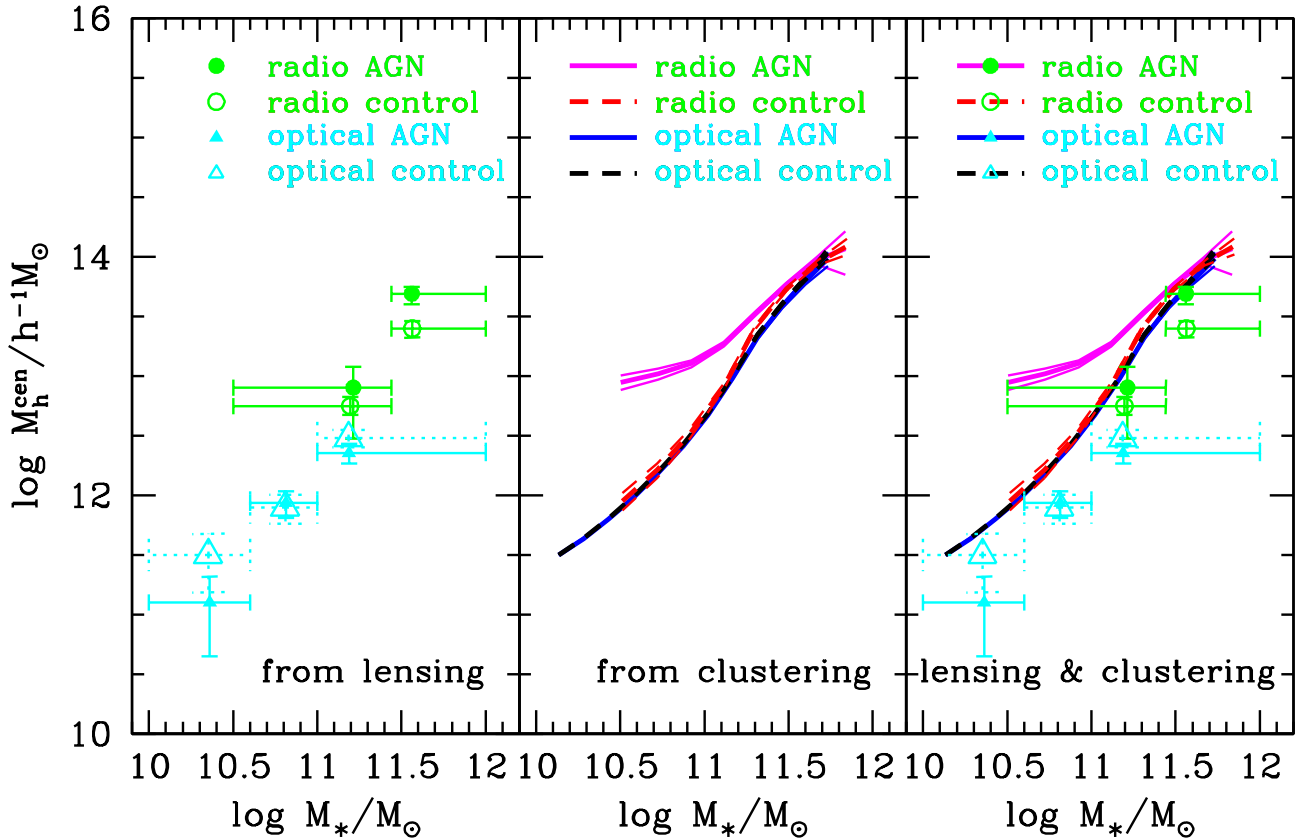
Figure 12. *Left*: Average central halo mass derived from galaxy-galaxy lensing is plotted as function of stellar mass, for three subsamples of optical AGN (cyan) and two subsamples of radio AGN (green). Filled symbols show results for the AGN samples, whole open symbols show results for the control samples. The stellar mass bin widths are indicated with horizontal errorbars. *Middle*: Average central halo mass derived from the clustering analysis is plotted as a function of stellar mass for optical (blue) and radio (magenta) AGN, and for the control galaxies (black dashed line for optical and red dashed for radio). *Right*: The results from the lensing and the clustering analyses are plotted on top of each other for comparison.

between the results for these two completely independent techniques is satisfactory, once we take into account the fact that (a) there is some modeling uncertainty in the best-fitting central halo masses from lensing due to the assumption of a narrow central halo mass distribution, and (b) the halo masses from the lensing analysis are relatively independent of the assumed σ_8 (which to lowest order only affects the best-fit α), but the halo masses from the clustering analysis are tied to $\sigma_8 = 0.9$ from the Millennium simulation through the large-scale bias - halo mass connection. In the latter case, we can estimate the effect of lowering σ_8 from 0.9, as in the mocks, to 0.8 (as in the WMAP 5-year results, Dunkley et al. 2008) at fixed $\Omega_m = 0.25$. Using the mass function from Tinker et al. (2008) at the typical redshift of radio AGN, and translating to our halo mass definition, we find that the requirement that the stellar mass function be matched, which is essentially an abundance constraint, would lead to the masses from the clustering analyses be lowered by ~ 15 per cent at $10^{13} h^{-1} M_\odot$, or ~ 25 per cent at $3 \times 10^{13} h^{-1} M_\odot$. While this difference is significant, it can only partially account for the differences shown in the figures. However, the modeling uncertainty due to the simple HOD used for the lensing analysis can lead to significant

additional uncertainty in those masses, typically leading to underestimation (i.e., the sign of the apparent discrepancy) by several tens of per cent when the central halo mass distributions are quite broad (Mandelbaum et al. 2005b), as is the case for several of our stellar mass subsamples (Figs. 3 and 9).

Putting the lensing and the clustering results together leads us to the following major conclusions:

• Radio AGN are hosted by galaxies with higher stellar masses than optical AGN, and are also in more massive dark matter halos. The mean stellar mass of the optical AGN sample is $8 \times 10^{10} M_\odot$ and the corresponding mean central halo mass deduced from galaxy-galaxy lensing is $(8.0 \pm 1.5) \times 10^{11} h^{-1} M_\odot$. The mean stellar mass of the radio AGN sample is $2.5 \times 10^{11} M_\odot$ and the mean halo mass deduced from galaxy-galaxy lensing is $(1.6 \pm 0.4) \times 10^{13} h^{-1} M_\odot$. Thus, the mean stellar mass and mean central halo mass for the radio AGN are ~ 3 and ~ 20 times the corresponding values for the optical AGN.

• At *fixed* stellar mass, radio-loud AGN inhabit more massive dark matter halos than optical AGN. This is seen both in the clustering and and in the galaxy-galaxy lensing analyses. Note that for the g-g lensing analysis, the high-
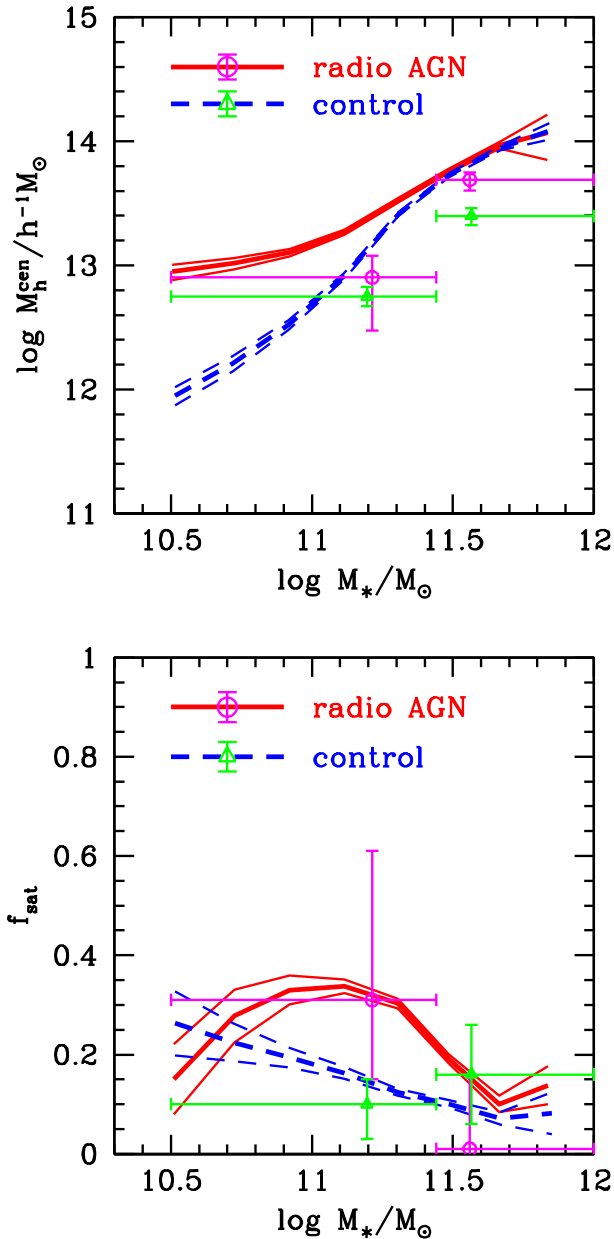
Figure 11. Mean halo mass for central radio AGN (upper panels) and satellite fraction of all radio AGN (lower panels) are plotted as function of stellar mass. In each panel, the red thick line shows the best-fitting model determined by the clustering measurements of radio AGN, and the blue thick line shows the result for control galaxies. The thin lines show the $1-\sigma$ variance between 200 mock catalogues. The results determined by the g-g lensing analyses are plotted as magenta circles for radio AGN and as green triangles for control galaxies; horizontal errorbars indicate the widths of the stellar mass bins.

est stellar mass bin for the optical AGN and the lowest bin for the radio-loud AGN have the same mean stellar mass. Fig. 12 shows that these two samples have very different halo masses. While the halo masses are also different for the control galaxies due to the morphology-dependence of halo mass at fixed stellar mass $> 10^{11} M_\odot$ (Mandelbaum et al.

2006), the difference is even more pronounced for the optical and radio-loud AGN samples.

• At *fixed* stellar mass, optical AGN inhabit dark matter halos of similar mass as galaxies of the same stellar mass selected without regard to AGN properties.

• At *fixed* stellar mass, radio-loud AGN inhabit more massive dark matter halos than galaxies of the same stellar mass selected without regard to AGN properties. We emphasize that despite the difficulty in representing this offset using our simple clustering model, it is present observationally at high significance in both the clustering data (Fig. 4) and the lensing data (Figs. 8 and 10) both for the full samples and for the two stellar mass subsamples.

• The clustering and lensing analyses together favour a model in which radio-loud AGN are not found in dark matter halos with masses less than about $3 \times 10^{12} h^{-1} M_\odot$, though the preference for this over a model with a minimum mass a factor of 10 smaller is only a 2σ difference given the size of current datasets.

One unresolved point in the reconciliation between the modeling of the clustering and its comparison with the lensing analysis is that the lensing analysis found the most significant difference between the central halo masses for radio AGN and controls at the high stellar mass end, whereas the clustering modeling suggests the largest difference should occur for lower stellar mass. This point is simply an artifact of overly simplistic modeling of a strict mass threshold, and may therefore be resolved with more sophisticated modeling involving a probability that is a function of mass; however, the introduction of more model parameters is not justified by the achievable S/N of the data at this time.

In Fig. 13, we compare the satellite fractions inferred by the two techniques. The results are broadly consistent with each other. The clustering analysis yields bigger differences in the inferred satellite fractions, particularly for AGN with low stellar masses. Optical AGN with low stellar masses are predicted to be quite strongly biased to central galaxy hosts, whereas radio AGN with low stellar masses are predicted to be located more frequently in satellite galaxies. The lensing analysis gives some weak indications of trends in the same direction, but the results are far from conclusive.

6 IMPLICATIONS OF THIS WORK

Perhaps the most important finding of this work is that optical AGN largely follow the same relation between stellar mass and halo mass as "ordinary" galaxies, but that radio-loud AGN deviate significantly from it (by a factor of ~ 2). This statement is true at the 97 per cent CL even if we restrict the analysis to those radio-loud AGN and control galaxies in the field (excluding those in massive groups and clusters).

This result implies that the large-scale halo environment plays an important role in understanding the radio AGN phenomenon. Previous work (e.g. Best et al. 2005a) has shown that the fraction of radio AGN increases strongly for more massive galaxies, suggesting that radio jets are more readily triggered in galaxies with more massive black holes. However, when we compare radio AGN with control galaxies of the same stellar mass selected without regard for nuclear activity, we find that the radio AGN reside in
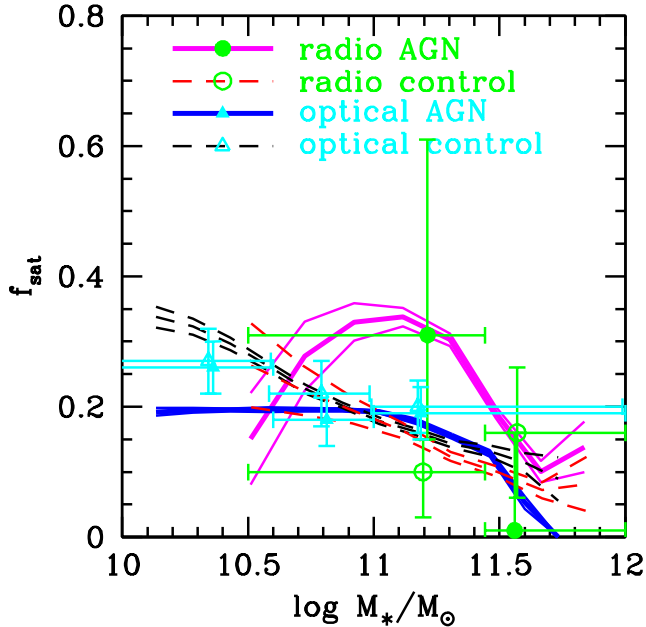
Figure 13. Satellite fraction as a function of stellar mass. Symbols and lines are the same as in the previous figure.

dark matter halos that are a factor of two more massive on average. This boost in halo mass appears to be *largely independent of luminosity of the radio source.* This demonstrates that black hole mass is not the only parameter that controls the radio AGN phenomenon – some aspect of the larger-scale environment of the galaxy must play a crucial role in regulating when the jet is switched on or when it is visible at radio wavelengths.

Recent semi-analytic models have assumed that feedback from radio AGN only becomes important in halos in which gas is cooling quasi-statically, i.e. halos above a mass of a few $\times 10^{11} - 10^{12} M_\odot$ (Croton et al. 2006; Bower et al. 2006; Cattaneo et al. 2006). Our clustering results strongly support this idea. Our two best-fitting HOD models both invoke a minimum halo mass close to these values, below which radio AGN are no longer found. If we do not impose a minimum mass, our models are not able to fit the observation correlation amplitude of radio-loud AGN on large scales.

Finally, the fact that the optical AGN in our sample follow the same $M_* - M_{halo}$ relation as the general galaxy population, implies that the optical AGN phenomenon is largely decoupled from the host halo. For the highest stellar mass bin, the best-fitting central halo mass derived from galaxy-galaxy lensing is more consistent with published results for late-type galaxies. This result is consistent with the general tendency of narrow-line AGN to be associated with galaxies with ongoing star formation and by extension, a cold interstellar medium.

REFERENCES

Abazajian K. et al. 2003, AJ, 126, 2081
Abazajian K. et al. 2004, AJ, 128, 502
Abazajian K. et al. 2005, AJ, 129, 1755
Adelman-McCarthy J. K. et al. 2006, ApJS, 162, 38
Adelman-McCarthy J. K. et al. 2007, ApJS, 172, 634
Adelman-McCarthy J. K. et al. 2008, ApJS, 175, 297
Bartelmann M., Schneider P., 2001, Phys.Rep., 340, 291
Becker R. H., White R. L., Helfand D. J., 1995, ApJ, 450, 559
Benson A. J., Baugh C. M., Cole S., Frenk C. S., Lacey C. G., 2000, MNRAS, 316, 107
Berlind A. A., Weinberg D. H., 2002, ApJ, 575, 587
Bernstein G. M., Jarvis M., 2002, AJ, 123, 583
Best P. N., Kauffmann G., Heckman T. M., Brinchmann J., Charlot S., Ivezić Ž., White S. D. M., 2005a, MNRAS, 362, 25
Best P. N., Kauffmann G., Heckman T. M., Ivezić Ž., 2005b, MNRAS, 362, 9
Best P. N., von der Linden A., Kauffmann G., Heckman T. M., Kaiser C. R., 2007, MNRAS, 379, 894

Blanton M. R., Brinkmann J., Csabai I., Doi M., Eisenstein D., Fukugita M., Gunn J. E., Hogg D. W., Schlegel D. J., 2003a, AJ, 125, 2348

Blanton M. R. et al. 2003b, ApJ, 592, 819

Blanton M. R., Lin H., Lupton R. H., Maley F. M., Young N., Zehavi I., Loveday J., 2003c, AJ, 125, 2276

Blanton M. R., Schlegel D. J., Strauss M. A., Brinkmann J., Finkbeiner D., Fukugita M., Gunn J. E., Hogg D. W., et al., 2005, AJ, 129, 2562

Bower R. G., Benson A. J., Malbon R., Helly J. C., Frenk C. S., Baugh C. M., Cole S., Lacey C. G., 2006, MNRAS, 370, 645

Cattaneo A., Dekel A., Devriendt J., Guiderdoni B., Blaizot J., 2006, MNRAS, 370, 1651

Condon J. J., Cotton W. D., Greisen E. W., Yin Q. F., Perley R. A., Taylor G. B., Broderick J. J., 1998, AJ, 115, 1693

Cooray A., Sheth R., 2002, Phys.Rep., 372, 1

Croom S. M., Boyle B. J., Shanks T., Smith R. J., Miller L., Outram P. J., Loaring N. S., Hoyle F., et al., 2005, MNRAS, 356, 415

Croton D. J., Springel V., White S. D. M., De Lucia G., Frenk C. S., Gao L., Jenkins A., Kauffmann G., et al., 2006, MNRAS, 365, 11

Dunkley J. et al. 2008, preprint (arXiv:0803.0586)

Eisenstein D. J. et al. 2001, AJ, 122, 2267

Finkbeiner D. P. et al. 2004, AJ, 128, 2577

Fukugita M., Ichikawa T., Gunn J. E., Doi M., Shimasaku K., Schneider D. P., 1996, AJ, 111, 1748

Gunn J. E. et al. 1998, AJ, 116, 3040

Gunn J. E. et al. 2006, AJ, 131, 2332

Heckman T. M., Kauffmann G., Brinchmann J., Charlot S., Tremonti C., White S. D. M., 2004, ApJ, 613, 109

Hennawi J. F. et al. 2006, AJ, 131, 1

Heymans C. et al. 2006, MNRAS, 371, L60

Hirata C., Seljak U., 2003, MNRAS, 343, 459

Hoekstra H., Hsieh B. C., Yee H. K. C., Lin H., Gladders M. D., 2005, ApJ, 635, 73

Hogg D. W., Finkbeiner D. P., Schlegel D. J., Gunn J. E., 2001, AJ, 122, 2129

Hopkins P. F., Hernquist L., Cox T. J., Di Matteo T., Martini P., Robertson B., Springel V., 2005a, ApJ, 630, 705

Hopkins P. F., Hernquist L., Martini P., Cox T. J., Robertson B., Di Matteo T., Springel V., 2005b, ApJ, 625, L71

Ivezić Ž. et al. 2004, Astronomische Nachrichten, 325, 583

Jing Y. P., Mo H. J., Boerner G., 1998, ApJ, 494, 1

Kauffmann G., Colberg J. M., Diaferio A., White S. D. M., 1999, MNRAS, 303, 188

Kauffmann G., Heckman T. M., Best P. N., 2008, MNRAS, 384, 953

Kauffmann G., Heckman T. M., Tremonti C., Brinchmann J., Charlot S., White S. D. M., Ridgway S. E., Brinkmann J., et al., 2003, MNRAS, 346, 1055

Kauffmann G., Nusser A., Steinmetz M., 1997, MNRAS, 286, 795

Koester B. P. et al. 2007a, ApJ, 660, 239

Koester B. P. et al. 2007b, ApJ, 660, 221

Li C., Jing Y. P., Kauffmann G., Börner G., Kang X., Wang L., 2007, MNRAS, 376, 984

Li C., Kauffmann G., Heckman T., Jing Y. P., White S. D. M., 2008a, MNRAS, 385, 1903

Li C., Kauffmann G., Heckman T. M., White S. D. M., Jing Y. P., 2008b, MNRAS, 385, 1915

Li C., Kauffmann G., Jing Y. P., White S. D. M., Börner G., Cheng F. Z., 2006a, MNRAS, 368, 21

Li C., Kauffmann G., Wang L., White S. D. M., Heckman T. M., Jing Y. P., 2006b, MNRAS, 373, 457

Lupton R. H., Gunn J. E., Ivezić Z., Knapp G. R., Kent S., 2001, in Harnden F. R., Jr., Primini F. A., Payne H., eds, ASP Conf. Ser. Vol. 238, Astronomical Data Analysis Software and Systems X. Astron. Soc. Pac., San Francisco, p. 269

Magliocchetti M., Maddox S. J., Hawkins E., Peacock J. A., Bland-Hawthorn J., Bridges T., Cannon R., Cole S., et al., 2004, MNRAS, 350, 1485

Mandelbaum R., Hirata C. M., Seljak U., Guzik J., Padmanabhan N., Blake C., Blanton M. R., Lupton R., Brinkmann J., 2005a, MNRAS, 361, 1287

Mandelbaum R., Tasitsiomi A., Seljak U., Kravtsov A. V., Wechsler R. H., 2005b, MNRAS, 362, 1451

Mandelbaum R., Seljak U., Kauffmann G., Hirata C. M., Brinkmann J., 2006, MNRAS, 368, 715

Mandelbaum R. et al. 2008, MNRAS, 386, 781

Myers A. D., Brunner R. J., Nichol R. C., Richards, G. T., Schneider D. P., Bahcall N. A., 2007a, ApJ, 658, 85

Myers A. D., Brunner R. J., Richards, G. T., Nichol R. C., Schneider D. P., Bahcall N. A., 2007b, ApJ, 658, 99

Myers A. D., Richards G. T., Brunner R. J., Schneider D. P., Strand N. E., Hall P. B., Blomquist J. A., York, D. G., 2008, ApJ, 678, 635

Overzier R. A., Röttgering H. J. A., Rengelink R. B., Wilman R. J., 2003, A&A, 405, 53

Padmanabhan N., White M., Norberg P., Porciani C., 2008, preprint (arXiv:0802.2105)

Peacock J. A., Smith R. E., 2000, MNRAS, 318, 1144

Peebles P. J. E., 1980, The large-scale structure of the universe. Research supported by the National Science Foundation. Princeton, N.J., Princeton University Press, 1980. 435 p.

Pier J. R., Munn J. A., Hindsley R. B., Hennessy G. S., Kent S. M., Lupton R. H., Ivezić Ž., 2003, AJ, 125, 1559

Porciani C., Norberg P., 2006, MNRAS, 371, 1824

Reyes R., Mandelbaum R., Hirata C. M., Bahcall N., Seljak U., 2008, preprint (arXiv:0802.2365)

Richards G. T. et al. 2002, AJ, 123, 2945

Seljak U., 2000, MNRAS, 318, 203

Shen Y. et al. 2007, AJ, 133, 2222

Smith J. A. et al. 2002, AJ, 123, 2121

Springel V., Di Matteo T., Hernquist L., 2005a, MNRAS, 361, 776

Springel V., White S. D. M., Jenkins A., Frenk C. S., Yoshida N., Gao L., Navarro J., Thacker R., et al., 2005b, Nature, 435, 629

Stoughton C. et al. 2002, AJ, 123, 485

Strauss M. A. et al. 2002, AJ, 124, 1810

Tinker J. L., Kravtsov A. V, Klypin A., Abazajian K., Warren M. S, Yepes G., Gottlober S., Holz D. E, 2008, preprint (arXiv:0803.2706)

Tremaine S., Gebhardt K., Bender R., Bower G., Dressler A., Faber S. M., Filippenko A. V., Green R., et al., 2002, ApJ, 574, 740

Tucker D. L. et al. 2006, Astronomische Nachrichten, 327, 821

Wang L., Li C., Kauffmann G., De Lucia G., 2006, MN-
  RAS, 371, 537
White S. D. M., Rees M. J., 1978, MNRAS, 183, 341
Yang X., Mo H. J., Jing Y. P., van den Bosch F. C., 2005,
  MNRAS, 358, 217
Yang X., Mo H. J., van den Bosch F. C., 2003, MNRAS,
  339, 1057
York D. G. et al. 2000, AJ, 120, 1579

This paper has been typeset from a TEX/ LATEX file prepared
by the author.